An integrated optic and acoustic (IOA) approach for measuring suspended sediment concentration in highly turbid environments

Lin, Jianliang; He, Qing; Guo, Leicheng; van Prooijen, Bram; Wang, Zhengbing

DOI
10.1016/j.margeo.2019.106062

Publication date
2020

Document Version
Accepted author manuscript

Published in
Marine Geology

Combining optical and acoustic sensors to obtain accurate and high-resolution profiles of suspended sediment concentration in highly turbid environments

Jianliang Lin[1, 2], Qing He[1, *], Leicheng Guo[1], Bram C. van Prooijen[2], Zhengbing Wang[1, 2, 3]

[1] State Key Laboratory of Estuarine and Coastal Research, East China Normal University, Shanghai, China

[2] Faculty of Civil Engineering and Geosciences, Delft University of Technology, Delft, The Netherlands

[3] Deltares, Delft, The Netherlands

*Corresponding author: Qing He, Email address: qinghe@sklec.ecnu.edu.cn

Postal address: R408, SKLEC, Zhongshan N. Road 3663, Shanghai 200062, China.

Phone number: +86 (021) 6223 3688

Highlights:

(1) A combination of ASM, OBS and ADV resolves the ambiguity problem of two possible SSCs for an OBS/ADV output.

(2) The integrated optic acoustic (IOA) approach enlarges the measurement range of OBS and ADV to 100s g/L.

(3) The IOA approach provides high-resolution (1 cm) SSC profiles by ASM.

(4) The IOA approach was successfully applied in the Yangtze Estuary with SSC > 10 g/L.

Abstracts:

Accurate measurement of suspended sediment concentration (SSC) in highly turbid environments has been a problem due to the signal saturation and attenuation. The saturation returns a limited measurement range, and the attenuation raises the ambiguity problem that a low optical/acoustic output could mean a low or high SSC. In this study, an integrated optic acoustic (IOA) approach is therefore proposed to (i) overcome the ambiguity problem; (ii) increase the measurement range to high SSC values; and (iii) obtain high-resolution SSC profiles. The IOA approach is a combination of Argus Suspension Meter (ASM), Optical Backscatter Sensor (OBS) and Acoustic Doppler Velocimeter (ADV). In this approach, ASM-derived SSC is preferred because of its lowest relative error, followed by OBS and ADV. The ASM can produce high-resolution (1 cm) SSC profile when it is not saturated (usually SSC < 9 g/L). When the ASM is saturated, the missing SSC is recovered by the OBS. Since the IOA approach solves the ambiguity problem in signal conversion, the measurement range of OBS and ADV can be extended to 100s g/L. The best way to use an ADV, however, is to have a rough estimation and assist in the OBS conversion. The IOA approach was tested in the Yangtze Estuary during the wet and dry season, respectively. Comparison between the SSC given by the IOA approach and in-situ water sampling indicates that the proposed IOA approach is reliable with a relative error of 17–34%. The observed high SSCs were up to 63 g/L. The measurements also show that the suspension is more concentrated in the benthic layer in the wet season, whereas in the dry season, the suspension is better mixed throughout the water column. To reduce the effects of particle size/composition, we suggest the usage of in-situ water samples or mixed bottom sediment for the sensor calibration. Accurate calibrations with the particle size/composition correction are expected to access a higher accuracy of the IOA approach in future research.

Keywords: *suspended sediment concentration; Optical Backscatter Sensor; Argus Suspension Meter; Acoustic Doppler Velocimeter; concentrated benthic suspension; Yangtze River Estuary*

1. Introduction

Suspended sediment concentration (SSC) is a critical parameter for understanding the transport of sediment and associated contaminants (Manning et al., 2010; Liang et al., 2013; Huettel et al., 2014; Burchard et al., 2018). SSC also limits the light availability and inhibits the primary production in lakes, rivers, estuaries and coastal waters (Yoshiyama and Sharp, 2006; Van Kessel et al., 2011). SSC can vary orders of magnitude over a small distance or a short period (Burchard et al., 2018; Ge et al., 2018). Accurate SSC measurements with a high spatial and temporal resolution, therefore, have significant implications for the management of ecology, biogeochemistry, and geomorphology. However, measuring high-resolution SSC in a simple, robust and efficient way is not straightforward, particularly in highly turbid environments.

Water sampling (e.g., suction/pumping) is a traditional, reliable and widely used method to measure in-situ SSC. The SSC from the water sample is generally regarded as a reference for the sensor calibration (Kineke and Sternberg, 1992; Fugate and Friedrichs, 2002; Gray and Gartner, 2010; Wang et al., 2013; Baeye and Fettweis, 2015; Druine et al., 2018). The SSC given by this method contains a relative error of ~ 20% from sampling and later analysis (McHenry et al., 1967). Point-integrating samplers can obtain SSC profiles of nearly the entire water column. However, water sampling is labor-intensive, implying that both temporal and spatial resolutions are generally limited. Accurate near-bed sampling (< 0.5 m) is furthermore challenging, although this region is of high interest for understanding sediment exchange processes.

To obtain high-resolution SSC profile, especially in the bottom boundary layer, more advanced technologies and sensors (optical or acoustic) have been developed in last decades(Wren et al., 2000; Thorne and Hanes, 2002; Rai and Kumar, 2015; Rymszewicz et al., 2017).

Optical sensors measure SSC by the strength of back- or side-scattered light, e.g., Optical Backscatter Sensor (OBS) (Campbell Scientific, 2018), Argus Suspension Meter (ASM) (Argus, 2014),YSI (YSI Incorporated, 2012), Fiber Optic In-stream Transmissometer (FIT) (Campbell et al., 2005) and HHU-LIOS (Shao and Maa, 2017). They can measure SSC at a high frequency (1-25 Hz) (Campbell Scientific, 2018), but their measurements are generally restricted to a single point in a fixed deployment. Stacked optical sensors (e.g., Argus Suspension Meter, ASM) were later developed and provide SSC profile with a vertical resolution of 1 cm (Vijverberg et al., 2011; Ge et al., 2018). Although multiple or moving optical sensors increase the spatial resolution of SSC measurements, they still require an intrusion in the flow, which may disturb the turbulence as well as the distribution of suspended sediment. Particle-size dependency is another drawback of the optical sensor. The reading of the same sensor may increase by as much as ten times for the same SSC with a smaller particle size (Ludwig and Hanes, 1990; Campbell Scientific, 2018). Therefore, continuous calibration against the in-situ SSC from water sampling is suggested (Maa et al., 1992; Nauw et al., 2014). Additionally, the optical output has an upper limit, because of the signal saturation (e.g., ASM) or attenuation (e.g., OBS). Within a low SSC (< 9 g/L), optical output increases nearly linearly with increasing SSC (Fig.1, see also Downing, 2006; Shao and Maa, 2017). Beyond a threshold, however, ASM output maintains at its maximum, and OBS output decreases with increasing SSC (Fig. 1). As a result, ASM has a limited measurement range, and OBS has an ambiguity problem in conversion. A low OBS output could mean a low or high SSC. Recently, a laser infrared optical sensor was developed by Hohai University (Nanjing, China, HHU-LIOS) with a measurement range up to 30 g/L (Shao and Maa, 2017). This extension of SSC range is a significant improvement, but it is still insufficient for the highly turbid environments, e.g., the Yangtze Estuary (Wan et al., 2014) and the EMS Estuary (Winterwerp et al., 2017). A combination of HHU-LIOS and OBS is therefore suggested by Shao and Maa (2017). However, their method only gives SSC at a single point.

Acoustic sensors are utilized for measuring SSC profiles non-intrusively, e.g., Acoustic Doppler Profiler (ADP) (Thorne and Hanes, 2002; Ha et al., 2011; Baeye and Fettweis, 2015) and Acoustic Doppler Velocimeter (ADV) (Ha et al., 2009; Salehi and Strom, 2011; Shao and Maa, 2017). In addition to SSC, acoustic sensors also measure flow velocity synchronously. ADP (Moura et al., 2011; Sahin et al., 2013; Fettweis and Baeye, 2015) and ADCP (Guerrero et al., 2011; Anastasiou et al., 2015; Baeye and Fettweis, 2015), for example, concurrently obtain velocity and SSC profiles over several meters. High-frequency acoustic signal (~ 10 Hz) can be used to estimate turbulent water/sediment flux, e.g., ADV (Fugate and Friedrichs, 2002; Scheu et al., 2015; Yang et al., 2016). Note that optical sensors cannot obtain synchronized high-frequency measurements of velocity at the same location, though they also provide high-frequency SSC estimates (Guo et al., 2018). The conversion from acoustic output into SSC also has the ambiguity problem and contains significant uncertainties. First, acoustic output increases exponentially with increasing and low SSC (< 1-2 g/L), so a small misalignment in acoustic output may introduce a significant error in its estimate. For instance, 1dB misalignment in ADV output can cause an error of ~ 1 g/L in the estimated SSC (Merckelbach and Ridderinkhof, 2006; Shao and Maa, 2017). Second, similar to optical sensors, the acoustic signal also attenuates in high SSC (> 1-10 g/L) (Fig. 2, see also Ha et al., 2009; Shao and Maa, 2017), which causes the ambiguity in SSC retrieval.

This study aims to solve the ambiguity problem that a low OBS/ADV reading could mean a low or high SSC and access a broader measurement range. We propose an integrated optic acoustic (IOA) approach to identify the "true" SSC and obtain high-resolution SSC profile by a combination of OBS, ASM and ADV. This paper is organized in the following way. Section 2 describes the calibration of sensors. Upon careful calibrations, we propose algorithms for each sensor to convert their outputs into SSC in Section 3. Compared with the SSCs from the water samples obtained in the Yangtze Estuary, these algorithms are evaluated. An optimal algorithm is then suggested in Section 4. The accuracy and advantages of the proposed IOA approach are discussed in Section 5. Section 5 also gives a discussion on the observed seasonal SSC profiles and intra-tidal bottom SSC variation in the Yangtze Estuary. It is concluded in Section 6, that the IOA approach is reliable, and it extends the measurement range to 100s g/L. The proposed IOA approach also provides high-resolution (1 cm) SSC profiles by the ASM when it is not saturated. The application of the IOA approach is beneficial for quantifying the sediment transport in the bottom boundary layer or highly turbid environments.

2. Sensor calibrations

The OBS (turbidity in NTU) and the ASM (turbidity in FTU) were calibrated in a cylindrical container (0.4 m diameter and 0.5 m height) with continuous and steady stirring at the bottom. First, the container was filled with the water collected from the Yangtze Estuary. To determine different SSC level, we gradually poured the slurry (an amalgam of bottom sediment collected every 2 hours within a campaign) into the container. The OBS and one of the ASM sensors (88^{th} sensor) were mounted at 15 cm above the bottom with an outlet at the same height for water sampling. At each SSC level, we took a water sample after the turbidity readings stabilized for 30 seconds. Subsequently, the water sample was filtered through a 0.45 μm filter and dried at 40 °C for 48 h to determine the SSC. Averaged turbidity during the sampling was then calibrated against the SSC of water sample (Fig. 1).

The calibration of ADV (signal-to-noise ratio, SNR in dB) was carried out with the in-situ SSC derived by ASM and OBS. The sampling rate of the ADV was 8 Hz, and the burst interval was 10 min. In each burst, the ADV sampled continuously for 90 seconds. In the signal processing, the SNR from three receiving transducers were averaged to obtain the representative mean value, and burst-averaged SNR was then calibrated with the in-situ SSC (Fig. 2).

Calibration results indicate that the response of each sensor (i.e., OBS, ASM and ADV) to increasing SSC is quite different. ASM turbidity (T_{ASM}) increases linearly with SSC below a limit of ~ 9 g/L (Figs. 1c and 1d). Beyond this limit, however, T_{ASM} maintains at the maximum (i.e., saturated). Figs. 1c and 1d also show that the sensors on the ASM behave roughly the same.

The OBS turbidity (T_{OBS}) shows three responses (Figs. 1a and 1b). (1) At low SSC where T_{ASM} is unsaturated, T_{OBS} increase is approximately linear. A critical OBS turbidity (T_C) can be determined when T_{ASM} just saturates (Fig. 3a). (2) Within a range of moderate SSC, where T_{ASM} saturates and $T_{OBS} \geq T_C$, T_{OBS} remains roughly the same and begins to decrease after reaching the maximum (max T_{OBS}). A parabolic function fits in this range. To relate the turbidity to SSC more directly, we divide the curve into two sections (Fig. 3a, curves 3 and 4). (3) T_{OBS} decreases linearly in high SSC where T_{ASM} saturates and $T_{OBS} < T_C$. After a process of trying to match the transition from one range to the next as continuous as possible, four curves are suggested as representative (Fig. 3a). Table 2 shows the equation for each calibration curve and their correlation coefficients.

The SNR from ADV also has three responses to different SSC level (Fig. 3b), i.e., increasing, constant and decreasing region. For convenience, parabolic fitting with SSC on a logarithmic scale is applied in this study, and it returns a high coefficient of determination (Table 2). Note that the max SNR occurs in a critical SSC (SSC_C = 2 g/L) (Fig. 2, see also Ha et al., 2009; Shao and Maa, 2017). It means that SNR decreases monotonically with SSC when ASM is saturated.

3. Conversion algorithms

Based on the different responses of ASM, OBS and ADV, algorithms are developed to convert their outputs into SSC (Fig. 4). To explain the conversion process, we take the OBS-633, ASM and ADV deployed in July 2014 as examples (Fig. 3).

The conversion of ASM is relatively simple. Before the conversion, whether the ASM is saturated or not needs to be identified. The ASM only provides estimates under unsaturated condition. Once the ASM saturates, no valid estimate is given by ASM. Fortunately, the missing high SSC can be recovered by the OBS or ADV.

The accurate conversion of OBS requires the assistance of ASM and ADV. Critical OBS turbidity (T_C) and SNR (SNR_C) need to be determined before the conversion (Fig. 3). When the T_{ASM} is not saturated, a second-order polynomial is applied (Fig. 3a, curve 2). For saturated T_{ASM} and $T_{OBS} < T_C$, the estimate is given by a negative and linear relationship (Fig. 3a, curve 5). For saturated T_{ASM} and $T_{OBS} \geq T_C$, however, the estimate is taken as the smaller solution to the parabolic equation when $SNR \geq SNR_C$ (Fig. 3a, curve 3) and the larger solution when $SNR < SNR_C$ (Fig. 3a, curve 4).

The SSC derived by ASM and OBS serves the conversion of ADV. High-frequency SSC (c) is a sum of burst-averaged ($\overline{c}$) and turbulent (c') components. Assuming that c does not change much within a sampling burst of 90 s (i.e., $c \approx \overline{c}$), we can identify the correct estimates of c by the $\overline{c}$ given by ASM and OBS. Upon the determination of critical SSC (SSC_C), the estimate is taken as the smaller solution to the parabolic equation when $SSC \le SSC_C$, (Fig. 3b, curve 6) and the larger solution when $SSC > SSC_C$ (Fig. 3b, curve 7).

4. Application and evaluation

To test and evaluate the proposed IOA approach and algorithms, we conducted field measurement campaigns in July 2014 and January 2016, respectively. Upon the comparison between the SSC given by each sensor and water sampling, an optimal algorithm is suggested within the IOA approach. This section also shows measured SSC profiles with and without such an algorithm and thus highlights the importance of using the IOA approach.

4.1 Field campaigns in the Yangtze Estuary

Since the surface SSC is up to 1 g/L and bottom SSC up to 10s g/L (He et al., 2001; Shi et al., 2006; Wan et al., 2014), the Yangtze Estuary is an excellent example of highly turbid water, particularly in the estuarine turbidity maximum (ETM). Two measurement campaigns were conducted in the ETM of the North Passage (Fig. 5). For each campaign, both tripod- and ship-borne systems with multiple sensors were employed. Table 3 shows the operated instruments and their sampling schemes.

A sketch of the bottom-mounted tripod system is given in Fig. 5d. An ASM measured turbidity profiles from 0.11 to 1.06 meter above the bed (mab here-after) with a vertical resolution of 1 cm. An OBS simultaneously measured turbidity, salinity, and temperature at 0.35, 0.55 and 1.06 mab, respectively. A downward-looking ADV recorded high-frequency 3D velocities and SNR at 0.35 mab. The sensors in the ADV were also used to monitor the heading, pitch and roll state of the tripod.

Ship-borne observations included measurements of turbidity, salinity and velocity profiles, and water sampling. Turbidity and salinity profiles were hourly measured by the OBS moved from water surface to near-bed (~ 0.5 m). The OBS stayed for 30 seconds at each relative depth layer, i.e., 0.05H (near-surface), 0.2H, 0.4H, 0.6H, 0.8H, and 0.95H (near-bed), where H is the total water depth. A water sample of 1.2 L was concurrently collected at each layer. These water samples were used for laboratory analysis of SSC, salinity and primary-particle-size distribution (PPSD). The PPSD was measured by the Coulter Counter analyzer after removing organic material and destroying flocs by sonification. An LISST-100 (type C) hourly recorded the in-situ floc-size distribution (FSD) and volume concentration at each layer. Bottom sediment was collected every 2 hours for the calibration of tripod-borne sensors.

To avoid interference between tripod- and ship-borne sensors, the tripod was deployed about 200 m upstream of the vessel. Compared with the distance between the two groins (~ 5 km), this distance is negligible. For safety reasons, it is not allowed to deploy an instrument tripod or mooring vessel in the Deepwater Navigational Channel (DNC). In our cases, both tripod- and ship-borne measurements were conducted at the south to the channel, about 200 m away from the DNC (Fig. 5c). Due to significant differences in cross-channel hydrodynamics and topography (Song et al., 2013; Wan et al., 2014; Ge et al., 2015), the tripod and the vessel should keep the same distance from the DNC. Therefore, we can assume that the tripod- and ship-borne measurements are representative for the same site, although they are actually in different locations.

Both temporal and spatial variations of temperature were small during the campaigns in July 2014 (24.7-27.0 ℃) and January 2016 (3.5-6.1 ℃). Hence the impact of temperature on the sensors was negligible within a campaign. Water temperature during the two campaigns, however, were significantly different from each other. The sensitivities of optical/acoustic sensors to SSC may change due to such a temperature difference. Therefore, we calibrated the sensors at the temperature similar to the on-site water temperature.

4.2 SSC from in-situ water samples

To evaluate the performance of each sensor, we regard the SSC from in-situ water sampling as the reference. During both campaigns, the water depth (H) ranged from 9 to 13 m (Figs. 6a and 7a), so the bottom SSC (at 0.95H) represented the SSC at 0.45-0.65 mab which can be used for the evaluation of tripod sensors. The SSC from water sample can only be verified by comparing samples taken closely in time and location. Unfortunately, such samples were not available in our study, so we cannot prove that an SSC from water sample is right or wrong. Note that the SSC may be incorrect due to sampling and analysis errors.

The SSC ranged 0.4-39.8 g/L during the campaign in July 2014 (Fig. 6d) and 1.4-5.1 g/L in January 2016 (Fig. 7d). High SSC and broad range in July 2014 are suitable to evaluate the performance of the proposed IOA approach in highly turbid environments. As a return, this approach benefits the detection of concentrated benthic suspension (CBS) where SSC > 10 g/L.

Concerning intra-tidal variation (Figs. 6d and 7d), the SSC increased directly after low water slack (LWS). An SSC peak occurred around the max flood, and the SSC decreased slightly then. After high water slack (HWS), the SSC increased rapidly again, reaching another peak on the early ebb. Subsequently, the SSC dropped and reached the minimum at LWS. Such an intra-tidal variation pattern is similar in the wet and dry season, except the higher SSC in the wet season and postponed peak in the late flood of the dry season.

On July 14, 15:00-17:00, the SSC from the water sample was more than 10 g/L (Fig. 6d). During this period, the ASM was saturated, and both the OBS and ADV outputs decreased significantly. It suggests that the observed high SSCs were reliable, and they caused optical/acoustic attenuation in the field, as reproduced by the in-lab calibration. On July 15, 2:00-5:00, however, the SSC decreased suddenly to ~ 1 g/L when the ASM was saturated. Meanwhile, the bottom turbidity was over 3000 NTU, validated by both tripod- and ship-borne OBS, indicating an SSC > 10 g/L. There are chances that the SSC from water sampling is underestimated during this period. This underestimation could be the result of (i) sampling not close enough to the bed; (ii) error of analysis in the laboratory; and (iii) a combination of both of the above. The underestimated SSC (only one sample) is therefore removed in the evaluation.

4.3 SSCs from OBS, ASM and ADV

During the observation in July 2014, the T_{ASM} saturated (with a reading around 4000 FTU) on the early ebb, which suggests a high SSC > ~ 9 g/L. Meanwhile, a significant reduction occurred in the T_{OBS} and SNR. Such responses of T_{ASM}, T_{OBS} and SNR to high SSC can be reproduced in the laboratory experiments (Figs. 1 and 2). It indicates that the response of each sensor is stable and reliable either in the lab or field.

By the proposed algorithms (Section 3), T_{ASM}, T_{OBS}, and SNR were converted into SSC. Figs. 6d (July 2014) and 7d (January 2016) show the time series of ASM-, OBS- and ADV-derived SSC at 0.35 mab. Note that the estimates given by the ASM are missing when it is saturated. All SSCs given by sensors follow the intra-tidal variation pattern of the SSC from the water sample. By the collaboration, OBS and ADV get access to higher SSC (> 60 g/L), although ASM only provides reliable estimates of SSC < 9 g/L.

The ADV also provides estimates of turbulent sediment flux ($\overline{w'c'}$). The observed $\overline{w'c'}$ had a tidally averaged magnitude of 10^{-4} kg/m^2/s and reasonable intra-tidal variation, similar to the theoretical calculations ($\frac{\upsilon_t}{\sigma_t}\frac{\partial c}{\partial z}$) (Fig. 8). υ_t is the eddy viscosity given by

$$\upsilon_t = \left(\overline{u'w'}\frac{\partial \bar{u}}{\partial z} + \overline{v'w'}\frac{\partial \bar{v}}{\partial z}\right)\left[\left(\frac{\partial \bar{u}}{\partial z}\right)^2 + \left(\frac{\partial \bar{v}}{\partial z}\right)^2\right]^{-1}. \qquad (1)$$

where σ_t is the turbulent Prandtl–Schmidt number, relating eddy viscosity (υ_t) to eddy diffusivity (K_t), as $K_t=\upsilon_t/\sigma_t$. A common assumption is that $\sigma_t = 0.7$. In highly turbid environments (e.g., the Yangtze Estuary), however, $\sigma_t = 2.0$ gives the optimal modeling of currents and SSC (Winterwerp et al., 2009). Direct comparison between the calculations ($\frac{\upsilon_t}{\sigma_t}\frac{\partial c}{\partial z}$) and in-situ measurements ($\overline{w'c'}$), verifies that $\sigma_t = 2.0$ gives a better estimate than $\sigma_t = 0.7$ (Fig. 8).

4.4 Optimal algorithm in the IOA approach

The performance of each sensor is evaluated by an averaged relative error:

$$Relative\ error = \overline{\frac{|C_{calculated} - C_{observed}|}{C_{observed}}} \times 100\% \qquad (2)$$

where $C_{calculated}$ is the SSC estimated by sensors based on the calibration curves (Table 2); $C_{observed}$ denotes to the SSC from the filtration of water sample (Druine et al., 2018).

Table 4 summarizes the relative error and measurement range of each sensor. ASM-derived SSC contains the lowest relative error (~ 25%), though it has limited measurement range (< 9 g/L). The ASM also provides high-resolution SSC profiles when it is not saturated. Our proposed algorithms successfully extend the measurement range of OBS to ~ 60 g/L, and OBS-derived SSC has a relative error of about 30%. Although the ADV has the most extensive measurement range (~ 360 g/L), its estimates contain the lowest accuracy (relative error > 80%), so the best it can be used is to have a rough estimation and assist in the conversion of OBS. According to the sensor performances, we suggest an optimal algorithm for the IOA approach (Fig. 4). ASM-derived SSC is preferred as long as the ASM is unsaturated. Under ASM-saturated condition, the missing ASM estimates can be recovered by the OBS. The main contribution of the ADV is to provide rough estimation and reduce the uncertainty in the OBS conversion.

4.5 Performance of the IOA approach

To highlight the importance and advantages of using the IOA approach with the optimal algorithm, Fig. 9 shows the estimated SSC profiles with and without the IOA approach. The classical method (i.e., without IOA approach) means that the SSC is estimated only by three OBSs at three different heights. By the OBS itself, the high-SSC-induced attenuation cannot be identified, so we can only conduct the conversion by the first stage of the calibration curve (e.g., curve 2 in Fig. 3). Therefore, the classical method may cause underestimation in high concentration.

Within low SSC (< 10 g/L), the two methods give similar SSC estimates (Fig. 9a). Closer to the bed, with increasing SSC, a difference appears between them (Figs. 9b and 9c). The SSC is significantly underestimated and generally less than 10 g/L without the IOA approach, whereas that estimated by the IOA approach is up to 63 g/L.

The ASM not only identifies the reliable estimates given by OBS but also provides high-resolution SSC profiles when it is not saturated (Figs. 9d, 9e and 9f). Ninety-six estimates are given in a profile with a vertical resolution of 1 cm. Without the IOA approach, however, only three estimates are given by the OBS at three layers (i.e., 0.35, 0.55 and 1.06 mab). When the near-bed high SSC appears, the IOA approach provides a more reasonable and reliable SSC profile. At 01:40 am, July 12 (Fig. 9d), for example, the proposed IOA approach gives an SSC of ~ 40 g/L at 0.35 mab, while an SSC of ~ 4 g/L is obtained without the IOA approach. The reliable SSC profile given by the ASM within 0.5-1.06 mab, suggests a sudden increase at 0.55 mab. Based on this trend, the SSC profile estimated by the IOA approach is more reasonable.

Upon careful calibration and conversion, the IOA approach with the optimal algorithm allows high temporal and vertical resolution of SSC variability. Particularly on the early ebb in July 2014, the CBS was successfully captured and measured. The observed CBS lasted 3-4 hours, and its thickness was ~ 1 m (Fig. 10c). The seasonal SSC variation was also observed in the Yangtze Estuary. In the wet season (Fig. 12a), the SSC profile is L-shaped with a much higher bottom SSC (up to 63 g/L). A significant SSC gradient is thus present in the lowest 0.2H. In the dry season (Fig. 12e), however, the SSC profile is more uniform over the entire water column. The SSC shows the highest value just above the bed and decreases almost linearly to the surface.

5. Discussion

5.1 Sources of relative errors

In this study, the SSC estimates given the ASM, OBS and ADV are evaluated by comparing with that from water sampling. Their relative errors are, therefore, not only determined by the sensor accuracy but also contaminated by the errors in water sampling and filtration.

The error from the sensor accuracy is unavoidable and accumulates in the relative error of the SSC estimate. OBS/ASM outputs, for example, have an accuracy of ± 10% (Argus, 2014; Campbell Scientific, 2018). Since a linear regression is applied for the ASM calibration, this accuracy causes a relative error of 10% in the ASM-derived SSC. For the OBS, this accuracy also leads to a relative error of 10% in the linearly increasing and decreasing region (i.e., curves 2 and 5 in Fig. 3a), and up to 90% around the turning point (i.e., curves 3 and 4 in Fig. 3a). The SNR is calibrated against the SSC on the logarithm scale, the relative error caused by its accuracy therefore increases with increasing SSC. Near the turning point (SSC = 2 g/L), for example, the SNR accuracy of ± 1% (Nortek, 2005) causes a relative error of 30%. The relative errors in Table 4, however, are higher than those caused by the sensor accuracy, which suggests additional sources for the given relative errors.

Note that no in-situ water sample was collected at the elevation (0.35 mab) where the ASM, OBS and ADV deployed, so we can only evaluate their SSC estimates with the water samples hourly obtained by a ship-borne sampler in the bottom layer (0.95H, i.e., ~ 0.45-0.65 mab). The relative errors could be thus overestimated because of the height difference between sensors and water samples, particularly when a large near-bed SSC gradient presents (e.g., July 2014). To obtain a more accurate relative error, we should employ a reliable in-situ water sampling system and collect water samples at the same elevation of sensors. Besides, the ADV was calibrated by the OBS-/ASM-derived SSC. Part of its relative error, therefore, may accumulate from those of the OBS/ASM. In other words, the relative error of ADV-derived SSC is also overestimated. We suggest an individual calibration for each sensor in future research.

Since the grain size and composition of suspended sediment can affect the responses of both optical and acoustic sensor (Conner and De Visser, 1992; Gibbs and Wolanski, 1992; Green and Boon, 1993; Merten et al., 2014; Su et al., 2016; Druine et al., 2018), their tidal variation could also introduce errors in the SSC estimates. In the Yangtze Estuary, characteristics of primary particles and flocs (e.g., size and density) continuously change in response to the complex advection, resuspension, deposition and flocculation processes (Guo et al., 2017). During the campaign in July 2014, the median grain size of primary particles (D_{P50}) ranged 4-20 µm, with an average of ~ 10 µm. Both the range and average enlarged in January 2016 (Table 5). Sediment composition, i.e., percentages of clay (P_{clay}), silt (P_{silt}) and sand (P_{sand}), varied with time and depth (Fig. 13 and Table 5). Table 5 also shows tidal averages of median floc size (D_{F50}) and floc density ($\rho = \bar{c}/V_c$, where $\bar{c}$ is the sediment concentration of water sample and V_c is the volume concentration measured by LISST) at each relative depth. In July 2014, for example, both D_{F50} (15-90 μm) and ρ (80-800 kg/m^3) had a broad range. Such strong variations in grain size and floc density could be one of the sources for the relative error of SSC estimates.

In this study, we reduce the effects of particle size/composition by using a mixture of bottom sediment for the sensor calibration. To a certain extent, the mixed bottom sediment represents the tidally averaged condition of suspended sediment in the bottom layer (Fig. 13). The calibration thus returns a representative curve for the averaged particle size/composition condition. Upon these calibrations, the proposed IOA approach gives SSC estimates with a relative error of 17–34%. This error is acceptable for in-situ SSC measurement and the quantification of sediment transport.

To access higher accuracy, one can introduce the particle size/composition correction in the calibration (Conner and De Visser, 1992; Fugate and Friedrichs, 2002; Green and Boon, 1993; Su et al., 2016). There are two basic methods, i.e., the "median grain size" method (Conner and De Visser, 1992) and the "mixture of linear component response" method (Green and Boon, 1993; Su et al., 2016). The former suggests corrections on the sensitivity coefficient as a function of the median grain size, but this method is highly empirical due to the controversial suggestions on empirical coefficients. By assuming that the total sensor output for mixtures is a linear sum of the output for each composition, the latter suggests to derive the sensitivity coefficients for different sediment compositions. Therefore, the "mixture of linear component response" method is recommended, because it thoughtfully considers the sensitivity of sensor response to each sediment composition.

5.2 Advantages and disadvantages of the IOA approach

By a combination of ASM, OBS and ADV, the proposed IOA approach successfully solves the ambiguity problem in conversion. Therefore, both OBS and ADV extend their measurement range of SSC (Table 4). Upon careful calibration, the OBS can provide estimates even up to 300 g/L (Kineke and Sternberg, 1992). Note that the estimation by ADV is not reliable, because of the rather scatter of data and the low SNR (Fig. 2). Although its measurement range can be extended to 100s g/L, the best way it can be used is to give a rough estimation and identify the true value from OBS-derived estimates. With the proposed optimal algorithm, we successfully captured and measured the CBS in the Yangtze Estuary.

In addition to solving the ambiguity problem and extending measurement range, the IOA approach also provides high-resolution SSC profiles by the ASM. In this study, the ASM was deployed on a tripod and measured the SSC profiles in the bottom boundary layer. These profiles have a higher resolution (0.01 m) than those measured by acoustic sensors (0.25-1.0 m), e.g., ADCP (Anastasiou et al., 2015; Baeye and Fettweis, 2015) and ADP (Fettweis and Baeye, 2015). Note that the ASM can produce valid high-resolution SSC profile only when it is not saturated. Once the ASM sensor is saturated, the estimate given by ASM is missing. These missing values, however, can be recovered by the OBS.

The IOA approach also provides direct and reliable measurements of turbulent sediment flux ($\overline{w'c'}$) by the ADV. Unlike optical sensors, the ADV provides estimates of turbulent velocity (w') and SSC (c') directly at the same position. In this method, the low-frequency SSC ($\overline{c}$) given by the ASM and OBS help to identify the reliable high-frequency estimate (c) by assuming $c \approx \overline{c}$ (i.e., $c' \approx 0$). This assumption is reasonable within a sampling burst of 90 s. Fig. 8 shows the ADV-derived $\overline{w'c'}$ with and without the IOA approach, as well as the theoretical calculations with σ_t = 0.7 and 2.0. Without the IOA approach, the $\overline{w'c'}$ is significantly underestimated (Fig. 8a). the $\overline{w'c'}$ with the IOA approach, however, maintains close to the theoretical calculation with σ_t =2.0, which is consistent to the observations by Cellino and Graf (1999) and modeling results by Winterwerp et al. (2009).

The IOA approach and the proposed optimal algorithm, however, have the following shortcomings. First, sensor responses to SSC are not entirely the same in the field and laboratory experiments. The OBS-633 employed in July 2014, for example, had a small amount (< 1%) of outputs during the field campaign that exceeded the maximum turbidity (3418 NTU) obtained in the in-lab calibration experiment. Part of the SSC given by the IOA approach is therefore missing. The tests by Maa et al. (1992) indicate that both clay mineralogy and salinity are important factors in the OBS calibration, whereas the scanning rate, the color of water and additional light source are not important. In our study, sediment samples used in the calibration were collected from the bed surface at the survey site. Their clay mineralogy thus did not change too much compared with the near-bed suspensions. The salinity, however, ranged 0-12‰ during the field measurement in July 2014, whereas the mixture of water samples returned a representative mean salinity of 5‰ in the in-lab calibration. Therefore, the salinity of ambient water is likely the main reason for the difference between the in-lab and in-filed response of an OBS. In-situ calibration is therefore recommended. Second, the effects of particle size/composition are not taken into account in the proposed algorithm. To improve the accuracy, careful calibrations with the particle size/composition correction are expected in future research.

5.3 Seasonal SSC profiles

The two studying periods (wet and dry seasons) show very different vertical SSC profiles (Figs. 12a and 12d). In the wet season, the SSC is higher in the benthic layer, but lower higher up in the water column; in the dry season, the opposite is found. Such a seasonality may correlate with the seasonal location of salinity wedge and ETM, estuarine stratification, floc size and settling velocity.

In the dry season, both the salinity wedge (Figs. 11b and 12f) and ETM (Wan, 2015; Fig. 7-12) locate further upstream, and thus the lower half of the water column may have a more uniform SSC profile, because of the thick salinity wedge and better mixing capability, especially the lowest 0.2H (Fig. 12e). In the wet season, the wedge moves to downstream, and only its head can reach the survey station (Figs. 10b and 12b). The observed wedge is therefore relatively thin, and the near-bed mixing is weak. As a result, the vertical SSC gradient is high near the bed. The thickness of this wedge is more than 2 m so that a high SSC gradient was observed at the experimental site. In other words, the near-bed SSC in the channel could be higher than that observed at the survey station.

In addition to wedge and ETM movement, the increasing freshwater discharge also enhances the strain-induced stratification (Simpson et al., 1990) and therefore estuarine circulation (Wan, 2015). The enhanced stratification benefits sediment trapping near the bottom (Geyer, 1993), while the circulation accumulates sediment in the convergent zone (i.e., ETM). As an overall result, both the SSC and its gradient are high near the bottom in the wet season. Although a stronger residual current (Figs. 12c and 12g) occurs in the wet season, depth-integrated sediment flux (Figs. 12d and 12h) is roughly the same. Because of the increasing sediment supply from the upstream (Guo et al., 2018), sediment accumulation therefore accelerates in the wet season, reaching a higher SSC.

The seasonality of SSC profile may also be the result of the changes in floc size and settling velocity. Both floc size and settling velocity are large in the wet season, and thus the suspension is more concentrated in the near-bed layer, because of the low turbulent shear (Wu et al., 2012) and high chlorophyll concentration (Fettweis and Baeye, 2015; Deng et al., 2019); and vice versa in the dry season. The quantification of the above processes should wait for the flocs, turbulence, and ETM data.

5.4 Intra-tidal SSC variation

Based on many in-situ and laboratory measurements, Maa and Kim (2002) and Ha and Maa (2009) found that erosion only occurs when the tidal current is in acceleration phases. This process may be used in this study to explain the observed intra-tidal SSC variation. Besides, the survey site locates on the land side to the tidally-averaged ETM (Wan, 2015; see Fig. 7-12), and thus horizontal advection may also contribute to the change of SSC time series, because of the large longitudinal and lateral SSC gradient.

During the flood periods in the wet season, the SSC increases with a reasonable pace whenever the current is accelerating (Fig. 6d). This slight increase may be attributed to the re-dispersion of new deposit from previous slack tides and the landward ETM movement. The SSC decreases slightly when the current starts decelerating. The cut-off of sediment supply from the bed and deposition in the late flood are responsible for this decrease. During ebb periods, the SSC jumps (or increases quickly) right after tidal current changes to acceleration phases. It suddenly decreases and recovers in 1-2 hours during this phase. There is a strong shoal-to-channel flow (Fig. 6b) for the decreasing SSC, and vice versa for the increase. It suggests that lateral flow controls the rapidly increasing or decreasing SSC during these periods. The SSC drops significantly right after the current starts decelerating, and remains about the same then. The withdrawal ETM (i.e., seaward movement) may predominate the rapid decrease, while the constant SSC is the result of limited sediment supply from the seabed.

In the dry season (Fig. 7d), the changes of SSC during the accelerating flood and the decelerating ebb have a similar pattern to those in the wet season. When the flood currents change to deceleration phases, however, the SSC first keeps increasing and then decreases gradually. During the accelerating ebb, a slight increase occurs in the beginning, followed by a slight decrease. Such variations during these two phases cannot be explained only by the asymmetric erosion/deposition, and longitudinal ETM movement may predominate these changes. Because of the low freshwater discharge, both salinity wedge and ETM can intrude further upstream. The ETM may even pass the observation station, leading to the increasing SSC during the decelerating flood. The decrease during the accelerating ebb may be the result of withdrawal ETM.

The difference between these two survey periods is probably caused by the different location and distribution of ETM. The ETM appears as a concentrated undercurrent in the wet season, and a low concentration sediment cloud in the dry season (Wu et al., 2012). A larger horizontal SSC gradient thus occurs in the wet season, especially in the cross-channel direction. In the branched Yangtze Estuary, the cross-channel current is caused by the barotropic force induced by the cross-shoal flow (Zhu et al., 2018). Although the cross-channel current is roughly the same during these two seasons (Figs. 6b and 7b), it provides a much stronger advective transport of SSC in the wet season, because of the larger SSC gradient. Such cross-channel transport of SSC is even stronger than that from the erosion of bottom sediment. At the ETM, both along- and cross-channel advection contribute significantly to the change of SSC, and thus, the observations of asymmetric erosion/deposition are not as clear as those observed by Maa and Kim (2002). More discussion/studies on the dominant process that controls intra-tidal SSC variation are needed, which should include detailed data on longitudinal and lateral distributions of ETM and current.

6. Conclusions

Due to the signal saturation, the ASM has a limited measurement range of SSC; both the OBS and ADV have an ambiguity problem in conversion because of the attenuation. By a combination of ASM, OBS, and ADV (i.e., the IOA approach), we successfully solve the ambiguity problem and access a broader measurement range and high-resolution SSC profiles. With this approach, the ASM-derived SSC is preferred because it has the lowest relative error (~ 25%). The ASM also provides high-resolution (1 cm) SSC profiles when it is not saturated (SSC < 9 g/L). Once the ASM is saturated, the estimates given by ASM is missing. These missing values, however, can be recovered by the OBS. Since the ambiguity problem is solved, both OBS and ADV extend their measurement range up to 100s g/L. Although the ADV has a more extensive SSC range, the best it can be used is to have a rough estimation and assist in the conversion of OBS output. To reduce the effects of particle size/composition, we suggest using in-situ water samples or mixed bottom sediment for the sensor calibration. Alternatively, one can take particle size/composition correction into account in the calibration to access a higher accuracy.

The application of the IOA approach successfully captured and measured the concentrated benthic suspensions (SSC > 10 g/L) in the Yangtze Estuary. Comparison between estimates and the SSC of the in-situ water sample indicates that the IOA approach is reliable and gives estimates with a relative error of 17–34%. The observed SSC profile in the Yangtze Estuary shows a notable seasonal variation. In the wet season, suspended sediment accumulates in the benthic layer, forming a non-uniform L-shaped profile, whereas a uniform and linear profile appears in the dry season.

Acknowledgments

The study was supported by the National Natural Science Foundation of China (grants 51320105005 and 51739005) and the project "Coping with deltas in transition" within the Programme of Strategic Scientific Alliances between China and The Netherlands (PSA), financed by the Chinese Ministry of Science and Technology (MOST), Project no. 2016YFE0133700 and Royal Netherlands Academy of Arts and Sciences (KNAW), Project no. PSA-SA-E-02. J.L. Lin is supported by the China Scholarship Council (CSC; grant 201706140180). We thank J. Gu, J. Zhao, L. Zhu, D. Zhang, C. Guo, Y. Chen, C. Xing, Z. Deng, J. Jiang, and Y. Shen for all technical aspects of instrumentation and moorings; R. Wu for help with the grain size analysis; and C. Zhu for useful discussion. We also appreciate the editor and two anonymous reviewers for their constructive and helpful comments that help to improve the manuscript.

References

Anastasiou, S., Sylaios, G.K., Tsihrintzis, V.A., 2015. Suspended particulate matter estimates using optical and acoustic sensors: application in Nestos River plume (Thracian Sea, North Aegean Sea). Environ. Monit. Assess. 187. https://doi.org/10.1007/s10661-015-4599-y

Argus, 2014. User Manual: Argus Suspension Meter V. Available Web at. http//argusnet.de/wp-content/uploads/2016/12/asm_V_reference.pdf.

Baeye, M., Fettweis, M., 2015. In situ observations of suspended particulate matter plumes at an offshore wind farm, southern North Sea. Geo-Marine Lett. 35, 247–255. https://doi.org/10.1007/s00367-015-0404-8

Burchard, H., Schuttelaars, H.M., Ralston, D.K., 2018. Sediment Trapping in Estuaries. Ann. Rev. Mar. Sci. 10, annurev-marine-010816-060535. https://doi.org/10.1146/annurev-marine-010816-060535

Campbell, C.G., Laycak, D.T., Hoppes, W., Tran, N.T., Shi, F.G., 2005. High concentration suspended sediment measurements using a continuous fiber optic in-stream transmissometer. J. Hydrol. 311, 244–253. https://doi.org/10.1016/j.jhydrol.2005.01.026

Campbell Scientific, I., 2018. Operator's Manual: OBS-3A Turbidity and Temperature Monitoring System. Available Web at. https//s.campbellsci.com/documents/us/manuals/obs-3a.pdf.

Cellino, M., Graf, W.H., 1999. Sediment-Laden Flow in Open-Channels under Noncapacity and Capacity Conditions. J. Hydraul. Eng. - ASCE 125, 455–462.

Conner, C.S., De Visser, A.M., 1992. A laboratory investigation of particle size effects on an optical backscatterance sensor. Mar. Geol. 108, 151–159. https://doi.org/10.1016/0025-3227(92)90169-I

Deng, Z., He, Q., Safar, Z., Chassagne, C., 2019. The role of algae in fine sediment flocculation: In-situ and laboratory measurements. Mar. Geol. 413, 71–84. https://doi.org/10.1016/j.margeo.2019.02.003

Downing, J., 2006. Twenty-five years with OBS sensors: The good, the bad, and the ugly. Cont. Shelf Res. 26, 2299–2318. https://doi.org/10.1016/j.csr.2006.07.018

Druine, F., Verney, R., Deloffre, J., Lemoine, J.P., Chapalain, M., Landemaine, V., Lafite, R., 2018. In situ high frequency long term measurements of suspended sediment concentration in turbid estuarine system (Seine Estuary, France): Optical turbidity sensors response to suspended sediment characteristics. Mar. Geol. 400, 24–37. https://doi.org/10.1016/j.margeo.2018.03.003

Fettweis, M., Baeye, M., 2015. Seasonal variation in concentration, size, and settling velocity of muddy marine flocs in the benthic boundary layer. J. Geophys. Res. Ocean. 120, 5648–5667. https://doi.org/10.1002/2014JC010644

Fugate, D.C., Friedrichs, C.T., 2002. Determining concentration and fall velocity of estuarine particle populations using adv, obs and lisst. Cont. Shelf Res. 22, 1867–1886. https://doi.org/10.1016/S0278-4343(02)00043-2

Ge, J., Shen, F., Guo, W., Chen, C., Ding, P., 2015. Estimation of critical shear stress for erosion in the Changjiang Estuary: A synergy research of observation, GOCI sensing and modeling. J. Geophys. Res. Ocean. 8439–8465. https://doi.org/https://doi.org/10.1002/2015JC010992 2

Ge, J., Zhou, Z., Yang, W., Ding, P., Chen, C., Wang, Z.B., Gu, J., 2018. Formation of Concentrated Benthic Suspension in a Time-Dependent Salt Wedge Estuary. J. Geophys. Res. Ocean. 1–27. https://doi.org/10.1029/2018JC013876

Geyer, W.R., 1993. The importance of suppression of turbulence by stratification on the estuarine turbidity maximum. Estuaries 16, 113–125. https://doi.org/10.1007/BF02690231

Gibbs, R.J., Wolanski, E., 1992. The effect of flocs on optical backscattering measurements of suspended material concentration. Mar. Geol. 107, 289–291. https://doi.org/10.1016/0025-3227(92)90078-V

Gray, J.R., Gartner, J.W., 2010. Technological advances in suspended-sediment surrogate monitoring. Water Resour. Res. 46. https://doi.org/10.1029/2008WR007063

Green, M.O., Boon, J.D., 1993. The measurement of constituent concentrations of non homogenous sediments suspension using optical backscatter sensors. Mar. Geol. 110, find pages.

Guerrero, M., Szupiany, R.N., Amsler, M., 2011. Comparison of acoustic backscattering techniques for suspended sediments investigation. Flow Meas. Instrum. 22, 392–401.

https://doi.org/10.1016/j.flowmeasinst.2011.06.003

Guo, C., He, Q., Guo, L., Winterwerp, J.C., 2017. A study of in-situ sediment flocculation in the turbidity maxima of the Yangtze Estuary. Estuar. Coast. Shelf Sci. 191, 1–9. https://doi.org/10.1016/j.ecss.2017.04.001

Guo, C., He, Q., van Prooijen, B.C., Guo, L., Manning, A.J., Bass, S., 2018. Investigation of flocculation dynamics under changing hydrodynamic forcing on an intertidal mudflat. Mar. Geol. 395, 120–132. https://doi.org/10.1016/j.margeo.2017.10.001

Guo, L., Su, N., Zhu, C., He, Q., 2018. How have the river discharges and sediment loads changed in the Changjiang River basin downstream of the Three Gorges Dam? J. Hydrol. 560, 259–274. https://doi.org/10.1016/j.jhydrol.2018.03.035

Ha, H.K., Hsu, W.Y., Maa, J.P.Y., Shao, Y.Y., Holland, C.W., 2009. Using ADV backscatter strength for measuring suspended cohesive sediment concentration. Cont. Shelf Res. 29, 1310–1316. https://doi.org/10.1016/j.csr.2009.03.001

Ha, H.K., Maa, J.P.Y., 2009. Evaluation of two conflicting paradigms for cohesive sediment deposition. Mar. Geol. 265, 120–129. https://doi.org/10.1016/j.margeo.2009.07.001

Ha, H.K., Maa, J.P.Y., Park, K., Kim, Y.H., 2011. Estimation of high-resolution sediment concentration profiles in bottom boundary layer using pulse-coherent acoustic Doppler current profilers. Mar. Geol. 279, 199–209. https://doi.org/10.1016/j.margeo.2010.11.002

He, Q., Li, J.F., Li, Y., Jin, X.S., Che, Y., 2001. Field measurements of bottom boundary layer processes and sediment resuspension in the Changjiang Estuary. Sci. China Ser. B-Chemistry 44, 80–86. https://doi.org/Doi 10.1007/Bf02884812

Huettel, M., Berg, P., Kostka, J.E., 2014. Benthic Exchange and Biogeochemical Cycling in Permeable Sediments. Ann. Rev. Mar. Sci. 6, 23–51. https://doi.org/10.1146/annurev-marine-051413-012706

Kineke, G.C., Sternberg, R.W., 1992. Measurements of high concentration suspended sediments using the optical backscatterance sensor. Mar. Geol. 108, 253–258. https://doi.org/10.1016/0025-3227(92)90199-R

Liang, D., Wang, X., Bockelmann-Evans, B.N., Falconer, R.A., 2013. Study on nutrient distribution and interaction with sediments in a macro-tidal estuary. Adv. Water Resour. 52, 207–220. https://doi.org/10.1016/J.ADVWATRES.2012.11.015

Ludwig, K.A., Hanes, D.M., 1990. A laboratory evaluation of optical backscatterance suspended solids sensors exposed to sand-mud mixtures. Mar. Geol. 94, 173–179. https://doi.org/10.1016/0025-3227(90)90111-V

Maa, J.P.Y., Kim, S.C., 2002. A Constant Erosion Rate Model for Fine Sediment in the York River, Virginia. Environ. Fluid Mech. 1, 345–360. https://doi.org/10.1023/A:1015799926777

Maa, J.P.Y., Xu, J., Victor, M., 1992. Notes on the performance of an optical backscatter sensor for cohesive sediments. Mar. Geol. 104, 215–218. https://doi.org/10.1016/0025-3227(92)90096-Z

Manning, A.J., Langston, W.J., Jonas, P.J.C., 2010. A review of sediment dynamics in the Severn Estuary: Influence of flocculation. Mar. Pollut. Bull. 61, 37–51. https://doi.org/10.1016/j.marpolbul.2009.12.012

McHenry, J.R., Coleman, N.L., Willis, J.C., Murphree, C.E., Bolton, G.C., Sansom, O.W., Gill, A.C., 1967. Performance of Nuclear-Sediment Concentration Gauges. Isot. Hydrol. 38, 207–225.

Merckelbach, L.M., Ridderinkhof, H., 2006. Estimating suspended sediment concentration using backscatterance from an acoustic Doppler profiling current meter at a site with strong tidal currents. Ocean Dyn. 56, 153–168. https://doi.org/10.1007/s10236-005-0036-z

Merten, G.H., Capel, P.D., Minella, J.P.G., 2014. Effects of suspended sediment concentration and grain size on three optical turbidity sensors. J. Soils Sediments 14, 1235–1241. https://doi.org/10.1007/s11368-013-0813-0

Moura, M.G., Quaresma, V.S., Bastos, A.C., Veronez, P., 2011. Field observations of SPM using ADV, ADP, and OBS in a shallow estuarine system with low SPM concentration-Vitória Bay, SE Brazil. Ocean Dyn. 61, 273–283. https://doi.org/10.1007/s10236-010-0364-5

Nauw, J.J., Merckelbach, L.M., Ridderinkhof, H., van Aken, H.M., 2014. Long-term ferry-based observations of the suspended sediment fluxes through the Marsdiep inlet using acoustic Doppler current profilers. J. Sea Res. 87, 17–29. https://doi.org/10.1016/j.seares.2013.11.013

Nortek, A.S., 2005. Technical Specification: Vector-300m. Available on Web at. https://www.nortekgroup.com/export/pdf/Vector%20-%20300%20m.pdf.

Rai, A.K., Kumar, A., 2015. Continuous measurement of suspended sediment concentration: Technological advancement and future outlook. Meas. J. Int. Meas. Confed. 76, 209–227. https://doi.org/10.1016/j.measurement.2015.08.013

Rymszewicz, A., O'Sullivan, J.J., Bruen, M., Turner, J.N., Lawler, D.M., Conroy, E., Kelly-Quinn, M., 2017. Measurement differences between turbidity instruments, and their implications for suspended sediment concentration and load calculations: A sensor inter-comparison study. J. Environ. Manage. 199, 99–108. https://doi.org/10.1016/j.jenvman.2017.05.017

Sahin, C., Safak, I., Hsu, T.J., Sheremet, A., 2013. Observations of suspended sediment stratification from acoustic backscatter in muddy environments. Mar. Geol. 336, 24–32. https://doi.org/10.1016/j.margeo.2012.12.001

Salehi, M., Strom, K., 2011. Using velocimeter signal to noise ratio as a surrogate measure of suspended mud concentration. Cont. Shelf Res. 31, 1020–1032. https://doi.org/10.1016/j.csr.2011.03.008

Scheu, K.R., Fong, D.A., Monismith, S.G., Fringer, O.B., 2015. Sediment transport dynamics near a river inflow in a large alpine lake. Limnol. Oceanogr. 60, 1195–1211. https://doi.org/10.1002/lno.10089

Shao, Y., Maa, J., 2017. Comparisons of Different Instruments for Measuring Suspended Cohesive Sediment Concentrations. Water 9, 968. https://doi.org/10.3390/w9120968

Shi, J.Z., Zhang, S.Y., Hamilton, L.J., 2006. Bottom fine sediment boundary layer and transport processes at the mouth of the Changjiang Estuary, China. J. Hydrol. 327, 276–288. https://doi.org/10.1016/j.jhydrol.2005.11.039

Simpson, J.H., Brown, J., Matthews, J., Allen, G., 1990. Tidal Straining, Density Currents, and Stirring in the Control of Estuarine Stratification. Estuaries 13, 125. https://doi.org/10.2307/1351581

Song, D., Wang, X.H., Cao, Z., Guan, W., 2013. Suspended sediment transport in the Deepwater Navigation Channel, Yangtze River Estuary, China, in the dry season 2009: 1. Observations over spring and neap tidal cycles. J. Geophys. Res. Ocean. 118, 5555–5567. https://doi.org/10.1002/jgrc.20410

Su, M., Yao, P., Wang, Z., Zhang, C., Chen, Y., Stive, M.J.F., 2016. Conversion of electro-optical signals to sediment concentration in a silt–sand suspension environment. Coast. Eng. 114, 284–294. https://doi.org/10.1016/j.coastaleng.2016.04.014

Thorne, P.D., Hanes, D.M., 2002. A review of acoustic measurement of small-scale sediment processes. Cont. Shelf Res. 22, 603–632. https://doi.org/10.1016/S0278-4343(01)00101-7

Van Kessel, T., Winterwerp, H., Van Prooijen, B., Van Ledden, M., Borst, W., 2011. Modelling the seasonal dynamics of SPM with a simple algorithm for the buffering of fines in a sandy seabed. Cont. Shelf Res. 31, S124–S134. https://doi.org/10.1016/j.csr.2010.04.008

Vijverberg, T., Winterwerp, J.C., Aarninkhof, S.G.J., Drost, H., 2011. Fine sediment dynamics in a shallow lake and implication for design of hydraulic works. Ocean Dyn. 61, 187–202. https://doi.org/10.1007/s10236-010-0322-2

Wan, Y., 2015. Multiscale physical processes of fine sediment in an estuary (PhD Thesis). Delft University of Technology, The Netherlands (198 pp.).

Wan, Y., Roelvink, D., Li, W., Qi, D., Gu, F., 2014. Observation and modeling of the storm-induced fluid mud dynamics in a muddy-estuarine navigational channel. Geomorphology 217, 23–36. https://doi.org/10.1016/j.geomorph.2014.03.050

Wang, Y.P., Voulgaris, G., Li, Y., Yang, Y., Gao, J., Chen, J., Gao, S., 2013. Sediment resuspension, flocculation, and settling in a macrotidal estuary. J. Geophys. Res. Ocean. 118, 5591–5608. https://doi.org/10.1002/jgrc.20340

Winterwerp, J.C., Lely, M., He, Q., 2009. Sediment-induced buoyancy destruction and drag reduction in estuaries. Ocean Dyn. 59, 781–791. https://doi.org/10.1007/s10236-009-0237-y

Winterwerp, J.C., Vroom, J., Wang, Z.B., Krebs, M., Hendriks, E.C.M., van Maren, D.S., Schrottke, K., Borgsmüller, C., Schöl, A., 2017. SPM response to tide and river flow in the hyper-turbid Ems River. Ocean Dyn. 67, 559–583. https://doi.org/10.1007/s10236-017-1043-6

Wren, B.D.G., Barkdoll, B.D., Kuhnle, R. a, Derrow, R.W., 2000. Field techniques for suspended-sediment measurement. J. Hydraul. Eng. 126, 97–104.

Wu, J., Liu, J.T., Wang, X., 2012. Sediment trapping of turbidity maxima in the Changjiang Estuary. Mar. Geol. 303–306, 14–25. https://doi.org/10.1016/j.margeo.2012.02.011

Yang, Y., Wang, Y.P., Gao, S., Wang, X.H., Shi, B.W., Zhou, L., Wang, D.D., Dai, C., Li, G.C., 2016. Sediment resuspension in tidally dominated coastal environments: new insights into the threshold for initial movement. Ocean Dyn. 66, 401–417. https://doi.org/10.1007/s10236-016-0930-6

Yoshiyama, K., Sharp, J.H., 2006. Phytoplankton response to nutrient enrichment in an urbanized estuary: Apparent inhibition of primary production by overeutrophication. Limnol. Oceanogr. 51, 424–434. https://doi.org/10.4319/lo.2006.51.1_part_2.0424

YSI Incorporated, 2012. User Manual: 6-Series, Multiparameter Water Quality Sondes. Available Web at. https//www.ysi.com/File%20Library/Documents/Manuals/ 069300-YSI-6-Series-Manual-RevJ.pdf. 374.

Zhu, L., He, Q., Shen, J., 2018. Modeling lateral circulation and its influence on the along-channel flow in a branched estuary. Ocean Dyn. 68, 177–191. https://doi.org/10.1007/s10236-017-1114-8

Table 1

Measurement techniques of suspended sediment concentration

Technology	Operating principle	Advantages	Disadvantages
Water sampling	Water-sediment sample is taken and later analyzed	Reliable Informative (SSC, salinity, PSD* etc.)	Flow-intrusive, Labor-intensive Low frequency Poor spatial resolution, Near-bed data missing
Optical	Light backscatter through water-sediment sample is measured and translated to SSC with calibration	High accuracy, Good spatial resolution High frequency	Flow-intrusive, Particle-size dependent, Limit measurement range Uncertainties in high SSC
Acoustic	Echo strength from sample determines SSC based on calibration	Nonintrusive, Good spatial resolution, High frequency synchronous SSC and velocity	Low accuracy, Limit measurement range Uncertainties in high SSC

* SSC and PSD denote suspended sediment concentration and particle size distribution, respectively.

Table 2

C-R relationship for calibrated sensors. C denotes suspended sediment concentration in g/L, and R represents the readings of OBS (turbidity in NTU), ASM (turbidity in FTU) and ADV (SNR in dB).

Time	Instrument	Conditions	C-R relationship	Number of samples	Correlation index (R^2)
201407	ASM	Unsaturated	$C=2.0\times10^{-3}R$	42	0.99
	OBS-633	Unsaturated	$C=3.5\times10^{-7}R^2+1.6\times10^{-3}R+0.2$	42	0.99
		Saturated, $T_{obs}\geq T_c$, $SNR\geq SNR_c$	$C=19.2-\frac{\sqrt{41734.0-12.2R}}{6.1}$	13	0.92
		Saturated, $T_{obs}\geq T_c$, $SNR<SNR_c$	$C=19.2+\frac{\sqrt{41734.0-12.2R}}{6.1}$		
		Saturated, $T_{obs}<T_c$	$C=-1.2\times10^{-2}R+66.0$	7	0.97
	OBS-636	Unsaturated	$C=3.0\times10^{-7}R^2+1.5\times10^{-3}R+0.2$	42	0.99
		Saturated, $T_{obs}\geq T_c$, $SNR\geq SNR_c$	$C=18.7-\frac{\sqrt{42531.8-11.7R}}{5.9}$	13	0.93
		Saturated, $T_{obs}\geq T_c$, $SNR<SNR_c$	$C=18.7+\frac{\sqrt{42531.8-11.7R}}{5.9}$		
		Saturated, $T_{obs}<T_c$	$C=-1.1\times10^{-2}R+65.9$	7	0.97
	OBS-638	Unsaturated	$C=3.9\times10^{-7}R^2+1.4\times10^{-3}R+0.1$	34	0.99
		Saturated, $T_{obs}\geq T_c$, $SNR\geq SNR_c$	$C=10.2-\frac{\sqrt{104937.2-35.0R}}{17.5}$	4	0.98
		Saturated, $T_{obs}\geq T_c$, $SNR<SNR_c$	$C=10.2+\frac{\sqrt{104937.2-35.0R}}{17.5}$		
		Saturated, $T_{obs}<T_c$	$C=-1.6\times10^{-2}R+59.2$	10	0.97
	ADV	$SSC\leq SSC_c$	$\lg C=0.3-\frac{\sqrt{2623.2-43.3R}}{21.7}$	685	0.70
		$SSC>SSC_c$	$\lg C=0.3+\frac{\sqrt{2623.2-43.3R}}{21.7}$		
201601	ASM	Unsaturated	$C=1.8\times10^{-3}R$	43	0.99
	OBS-278	Unsaturated	$C=6.9\times10^{-7}R^2+6.5\times10^{-4}R+0.2$	43	0.99
		Saturated, $T_{obs}\geq T_c$, $SNR\geq SNR_c$	$C=11.5-\frac{\sqrt{80551.5-27.5R}}{13.7}$	9	0.99
		Saturated, $T_{obs}\geq T_c$, $SNR<SNR_c$	$C=11.5+\frac{\sqrt{80551.5-27.5R}}{13.7}$		
		Saturated, $T_{obs}<T_c$	$C=-1.6\times10^{-2}R+61.1$	14	0.99
	OBS-279	Unsaturated	$C=3.2\times10^{-7}R^2+8.2\times10^{-4}R+0.2$	43	0.99
		Saturated, $T_{obs}\geq T_c$, $SNR\geq SNR_c$	$C=11.6-\frac{\sqrt{176062.0-45.0R}}{22.5}$	9	0.99
		Saturated, $T_{obs}\geq T_c$, $SNR<SNR_c$	$C=11.6+\frac{\sqrt{176062.0-45.0R}}{22.5}$		
		Saturated, $T_{obs}<T_c$	$C=-1.1\times10^{-2}R+57.0$	14	0.99
	OBS-570	Unsaturated	$C=6.0\times10^{-7}R^2+9.1\times10^{-4}R+0.2$	43	0.99

Saturated, $T_{obs} \geq T_c$, SNR≥SNR_c	$C=11.4-\frac{\sqrt{81988.4-28.0R}}{14.0}$	9	0.99
Saturated, $T_{obs} \geq T_c$, SNR<SNR_c	$C=11.4+\frac{\sqrt{81988.4-28.0R}}{14.0}$		
Saturated, $T_{obs} < T_c$	$C=-1.5\times10^{-2}R+56.1$	14	0.99

Table 3

Shipboard and tripod instruments and their sampling schemes

Carrier	Instrument deployed	Distance above bed (mab)	Sampling interval (min)	Sampling duration (sec)	Sampling frequency (Hz)	Survey parameter	Profile resolution (m)
Vessel	ADCP	> 1.5	continuously	continuously	0.1	upper velocity	0.5
	OBS	> 1.0	60	30	1	SSC, salinity, temperature	0.1
	LISST	*	60	30	1	FSD	-
	Water sampler	*	60	30	-	SSC, salinity, PPSD	-
Tripod	ACP	< 0.8	5	60	1	near-bed velocity	0.05
	ADCP-wave	> 2.0	5	60	1	upper velocity, wave	0.5
	RBR	1.1	5	60	1	wave	-
	ADV	0.35	10	60	8	near-bed velocity, SSC	-
	ASM	0.11-1.06	5	60	1	SSC	0.01
	OBS	0.35, 0.55, 1.06	5	60	1	SSC, salinity, temperature	-

* data or samples collected at six relative depth layers, i.e., 0.05H (near surface), 0.2H, 0.4H, 0.6H, 0.8H, and 0.95H (near-bed), where H is the total water depth. FSD and PPSD denote the flocculated and primary particle size distribution, respectively.

Table 4

Measurement ranges (g/L) of ASM, OBS and ADV with their relative errors (%). Missing values are represented by the symbol NA (Not Available).

Time	Instrument	Range (g/L)	Relative error (%)
201407	ASM	0.0-8.0	33.6
	OBS-633	0.2-66.0	32.2
	OBS-636	0.2-65.9	NA
	OBS-638	0.1-59.2	NA
	ADV	0.1-457.3	88.6
201601	ASM	0.0-7.4	17.6
	OBS-278	0.2-61.1	28.2
	OBS-279	0.2-57.0	NA
	OBS-570	0.2-56.1	NA

Table 5

Tidally averaged median grain sizes of primary particles (D_{P50}) and flocculates (D_{F50}), dry density (ρ) of flocculates and composition of suspended sediment in different layers with their standard deviations. Data are not available in the bottom layer as LISST does not work correctly in high turbidity. Missing values are represented by the symbol NA (Not Available).

TIME [yymm]	Position	D_{P50} (std.) [μm]	D_{F50} (std.) [μm]	ρ (std.) [kg/m^3]	P_{clay} (std.) [%]	P_{silt} (std.) [%]	P_{sand} (std.) [%]
1407	0.05H	6.0(±1.4)	26.3(±8.8)	310(±84)	39(±6)	56(±8)	5(±6)
	0.2H	7.3(±2.1)	24.7(±7.4)	311(±91)	35(±6)	61(±7)	4(±4)
	0.4H	8.9(±3.3)	25.7(±10.7)	304(±130)	32(±6)	64(±4)	4(±4)
	0.6H	10.4(±4.0)	27.5(±16.3)	275(±82)	30(±5)	65(±3)	5(±5)
	0.8H	11.6(±4.2)	33.9(±19.5)	238(±78)	28(±5)	66(±2)	6(±5)
	0.95H	13.5(±6.0)	33.3(±6.3)	246(±42)	27(±6)	63 (±3)	10(±7)
	Bed	12.1(±2.7)	NA	NA	27(±3)	64(±5)	9(±3)
	All samples	9.8(±4.5)	27.6(±12.8)	288(±97)	32(±7)	62(±6)	6(±5)
1601	0.05H	9.4(±4.0)	23.7(±5.4)	502(±339)	31(±7)	66(±6)	2(±2)
	0.2H	12.6(±5.8)	NA	NA	27(±6)	69(±4)	4(±3)
	0.4H	14.6(±5.2)	NA	NA	25(±5)	71(±3)	4(±3)
	0.6H	16.2(±5.0)	NA	NA	22(±4)	72(±2)	6(±4)
	0.8H	18.6(±5.4)	NA	NA	21(±4)	71(±3)	8(±4)
	0.95H	21.1(±5.9)	NA	NA	19(±4)	71(±3)	10(±5)
	Bed	26.7(±11.6)	NA	NA	17(±5)	65(±5)	18(±10)
	All samples	16.2(±7.6)	NA	NA	24(±7)	70(±4)	6(±6)

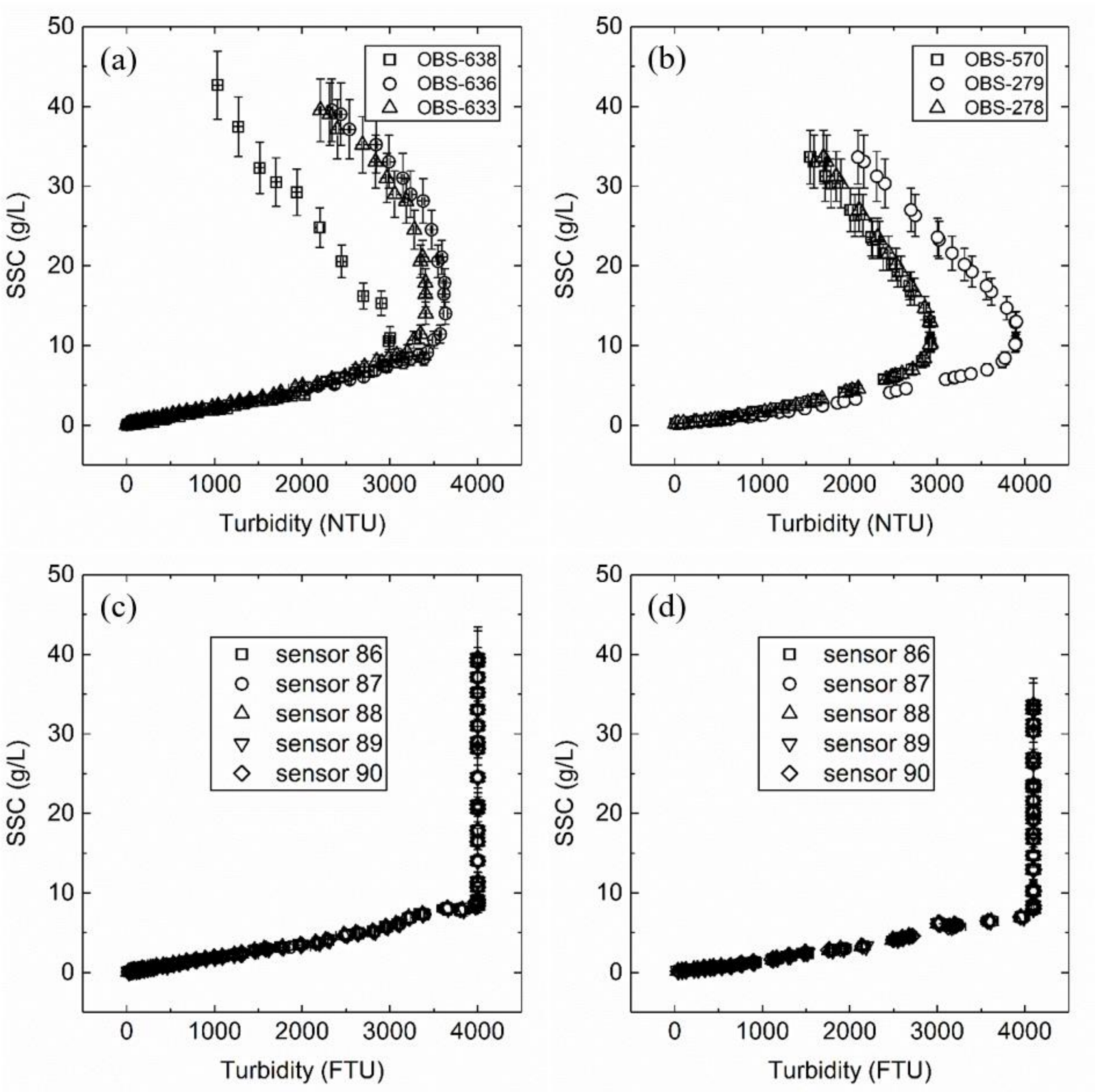

Figure 1. Calibrations of OBS (turbidity in NTU) (a, b) and ASM (turbidity in FTU) (c, d) against SSC (in g/L) with bottom sediment collected in July 2014 (left panel) and January 2016 (right panel), respectively. Regression results are shown in Table 2.

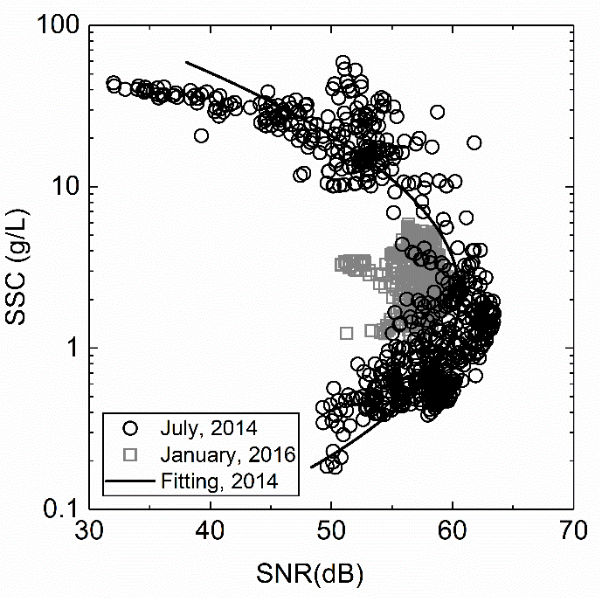

Figure 2. Calibration of ADV (SNR in dB) against the SSC (in g/L) given by ASM and OBS. Regression results are shown in Table 2.

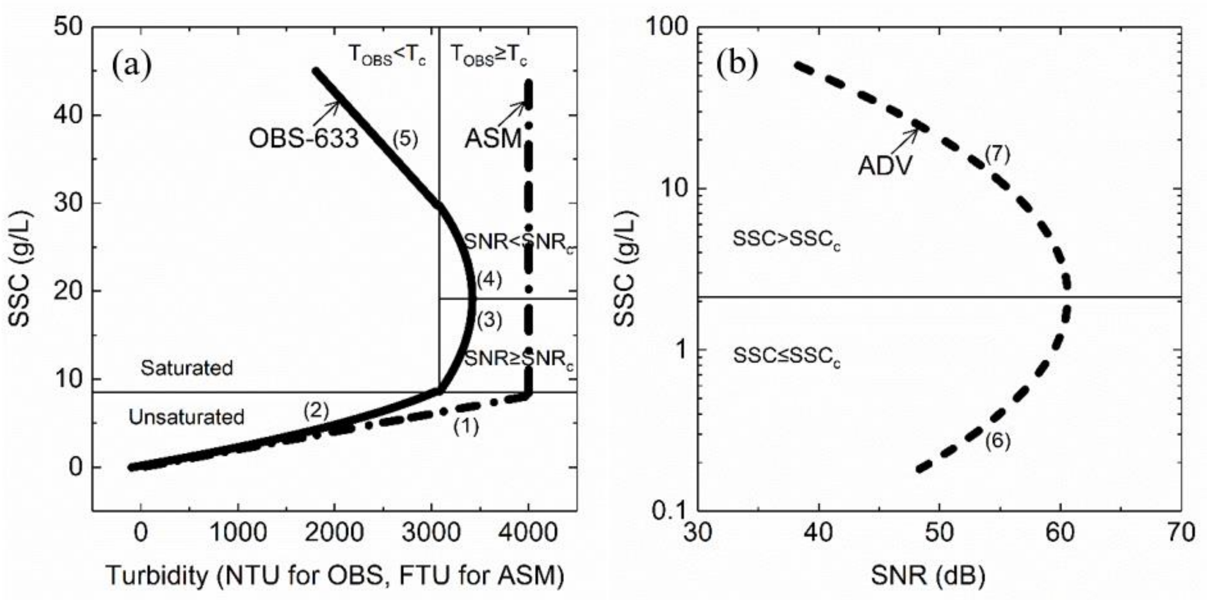

Figure 3. Examples of calibration curve (ASM, OBS-633 and ADV employed in July 2014) for illustrating the conversion protocols of the IOA approach. T_C denotes the critical OBS turbidity (reading, i.e., T_C =3050 NTU, corresponding to SSC ~ 9 g/L) where ASM just saturates (with a reading around 4000 FTU), and SNR_C (~ 61 dB) indicates the critical SNR corresponding to the max OBS turbidity (reading, i.e., 3400 NTU, corresponding to SSC = 20 g/L when using OBS. SSC_C indicates the critical SSC (i.e., SSC_C = 2 g/L) where the ADV returns the max SNR. The numbers in parenthesis, e.g., (4), is a shorthand of Calibration Relation (CR) 4 as shown in Table 2 and Figure 4.

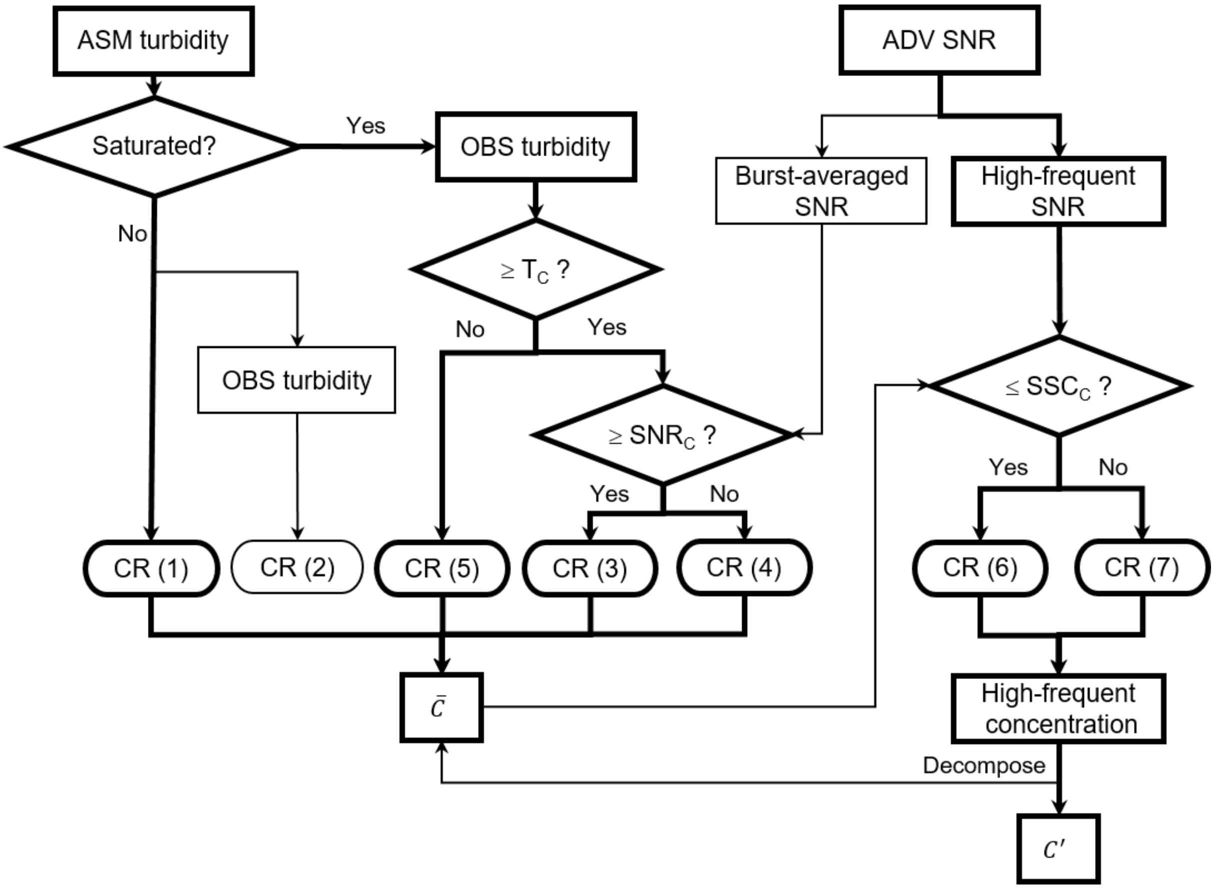

Figure 4. Algorithms for ASM, OBS and ADV to estimate reliable SSC. CR denotes the calibration relationship between suspended sediment concentrations and readings of sensors (i.e., turbidity and SNR) given in Table 2. Highlighted flowcharts show the optimal protocol according to the performance of each sensor.

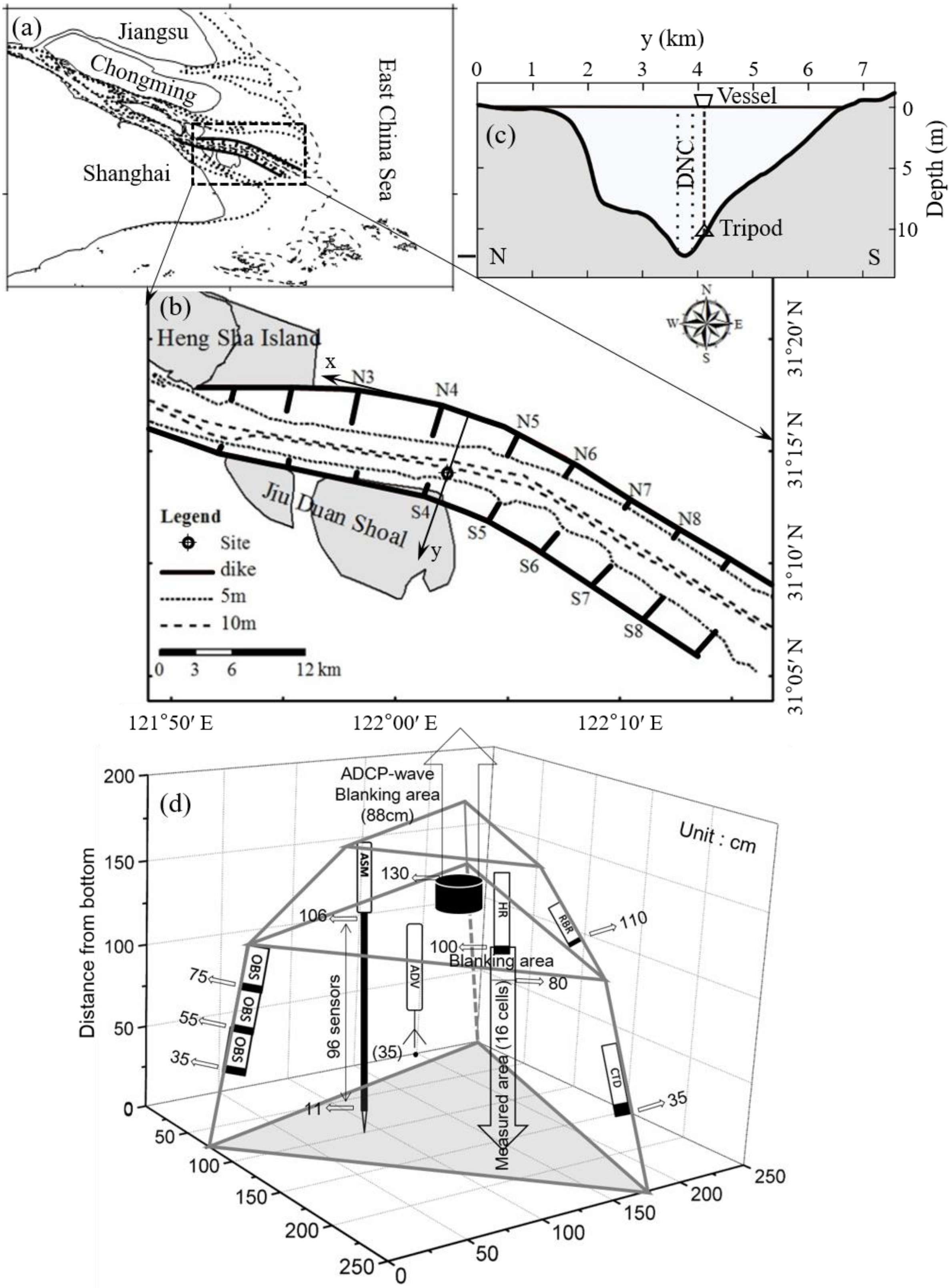

Figure 5. The Yangtze Estuary (a), the Deepwater Navigational Channel (DNC) at the North Passage (b), the positions of the DNC and the moored tripod and shipboard observation systems in an estuarine cross section (c), and the schematic of bottom-mounted tripod system with multiple sensors (d). The numbers in (d) represent the distance of the sensor above the seabed.

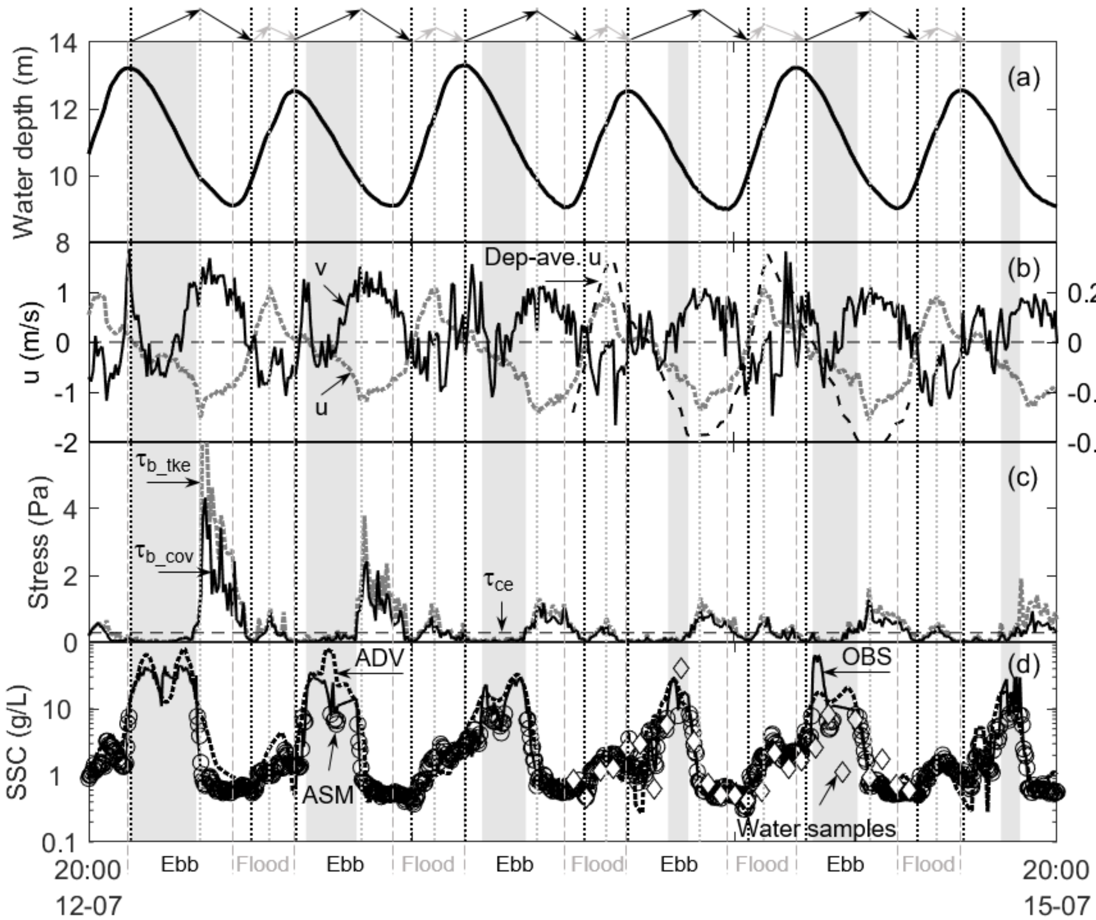

Figure 6. Time series of 2014 July (wet season) measurements in the North Passage, Yangtze Estuary. (a) water depth measured by the CTD, (b) along- (u, grey dot) and cross- (v, black solid) channel velocity measured by the ADV at 0.35 meter above bed (mab) and depth-averaged u (black dash); (c) bed stress calculated by TKE Method (τ_{b_tke}, grey dot) and COV Method (τ_{b_cov}, black solid) and critical stress for erosion (τ_{ce}, black dash); (d) SSCs from the filtration of water samples collected at the bottom layer (i.e., 0.95H, diamond), and ASM (circle), OBS (solid) and ADV (dot) at 0.35 mab. Positive u indicates the flood direction, and positive v represents the cross-channel velocity from the north to the south. Since the survey site locates at the south to the channel, positive v also indicates the channel-to-shoal flow. The time period for flood (grey) and ebb (black) are marked at the bottom. The tidal current acceleration phases are marked on top by arrows with a positive slope, and the deceleration phases are marked by arrows with a negative slope. The shadow area indicate the periods when SSC > 10 g/L. The tidal current phase between near-bed and depth-averaged velocity is roughly the same.

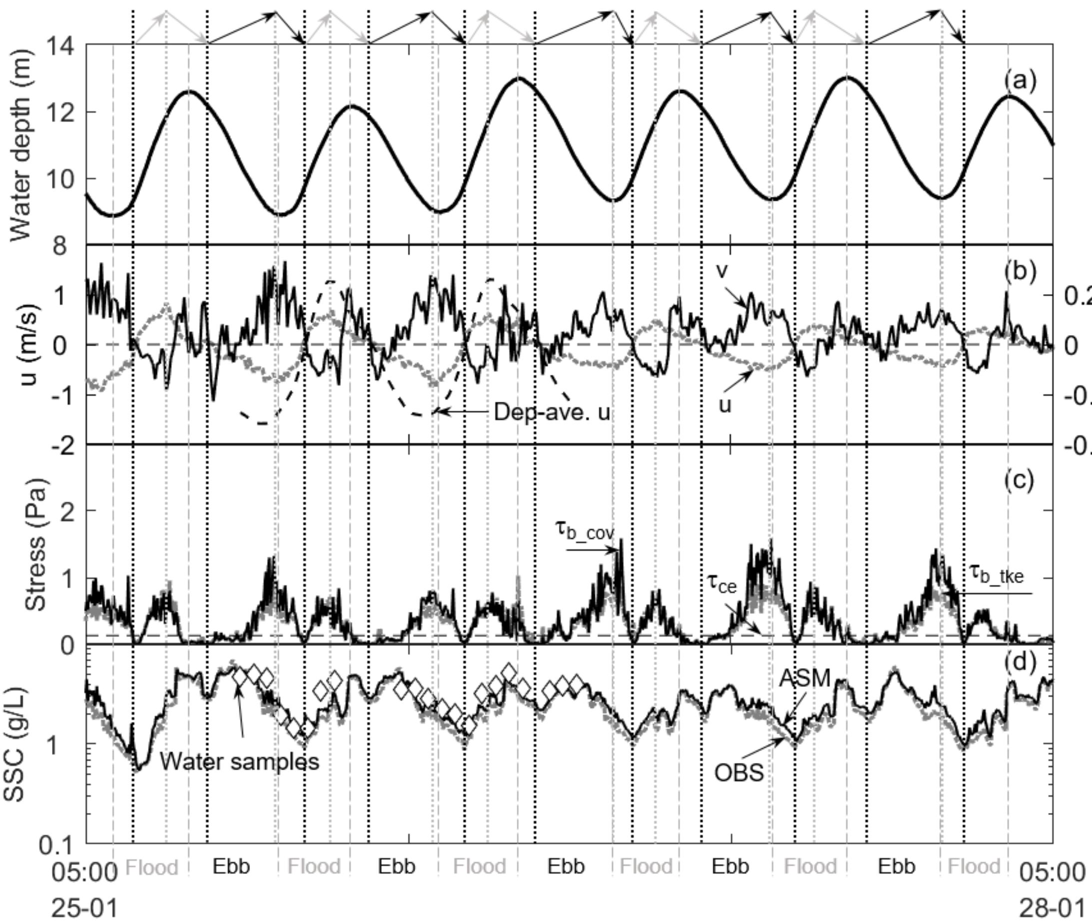

Figure 7. Time series of 2016 January (dry season) measurements in the North Passage, Yangtze Estuary. (a) water depth measured by the CTD, (b) along- (u, grey dot) and cross- (v, black solid) channel velocity measured by the ADV at 0.35 meter above bed (mab) and depth-averaged u (black dash); (c) bed stress calculated by TKE Method (τ_{b_tke}, grey dot) and COV Method (τ_{b_cov}, black solid) and critical stress for erosion (τ_{ce}, black dash); (d) SSCs from the filtration of water samples collected at the bottom layer (i.e., 0.95H, diamond), and ASM (solid) and OBS (grey dot) at 0.35 mab. Positive u indicates the flood direction, and positive v represents the cross-channel velocity from the north to the south. Since the survey site locates at the south to the channel, positive v also indicates the channel-to-shoal flow. The time period for flood (grey) and ebb (black) are marked at the bottom. The tidal current acceleration phases are marked on top by arrows with a positive slope, and the deceleration phases are marked by arrows with a negative slope. The tidal current phase between near-bed and depth-averaged velocity is roughly the same.

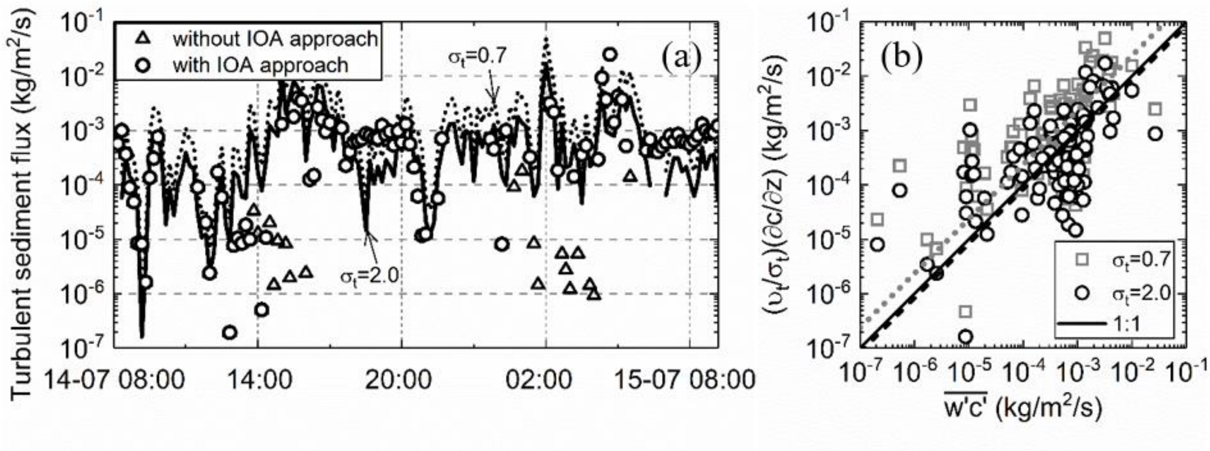

Figure 8. Comparison between ADV-derived turbulent sediment flux ($\overline{w'c'}$) and the theoretical calculations ($\frac{\upsilon_t}{\sigma_t}\frac{\partial c}{\partial z}$) with two classic values of turbulent Prandtl–Schmidt number, i.e., σ_t = 0.7 and σ_t = 2.0. ADV-derived $\overline{w'c'}$ with and without the proposed algorithm are also presented (a).

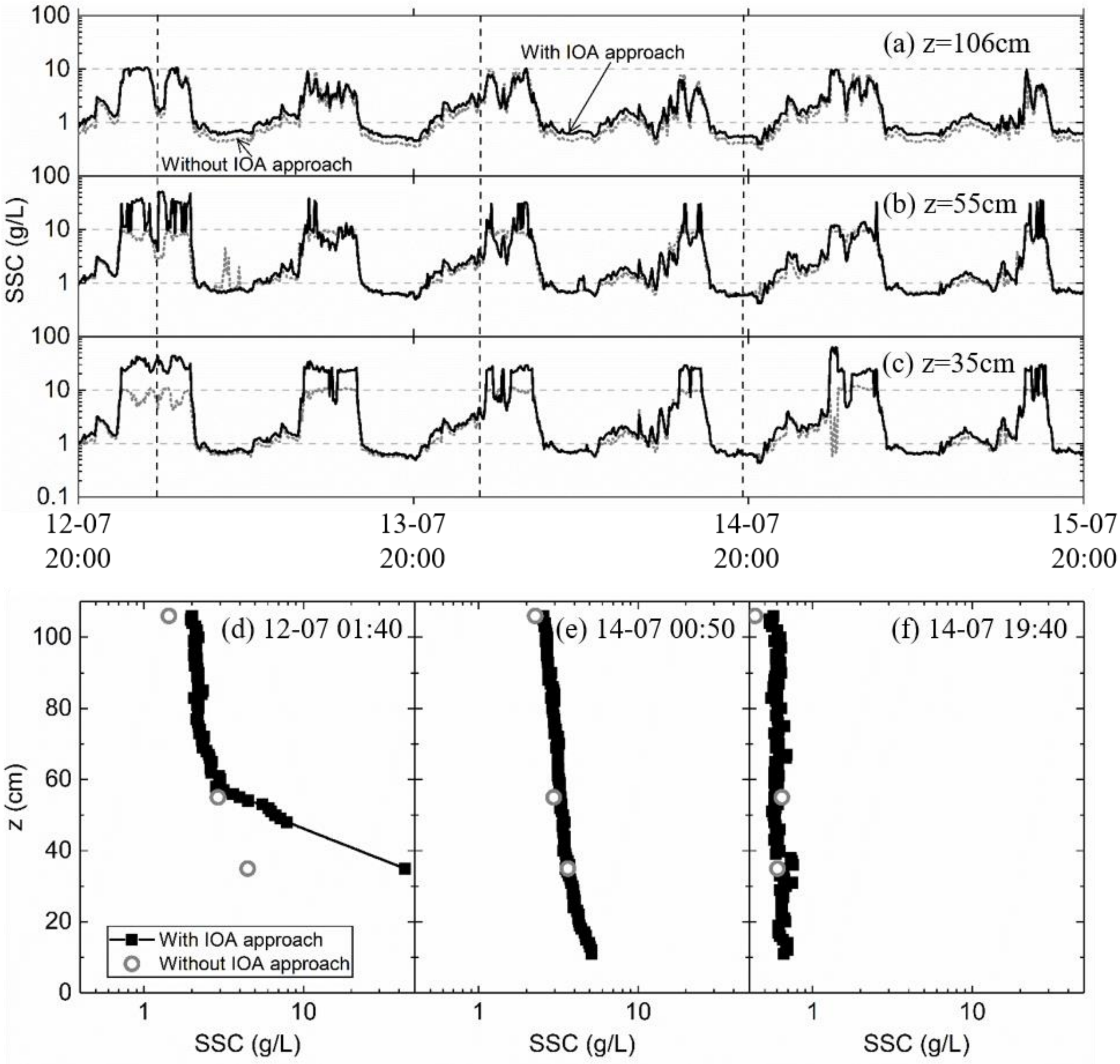

Figure 9. Time series of SSC from three tripod mounted OBSs with (black solid) and without (grey dot) the IOA approach at 106 cm (a), 55 cm (b) and 35 cm (c) above bed, and three representative SSC profiles within high (d), mid (e) and low (f) SSC. The ASM readings below 50 cm from bed are saturated (d), and thus, removed, except the one at 35 cm above bed, which was recovered by the OBS reading at that time. A straight line between the SSCs from ASM at 35 and 50 cm is suggested as the possible SSC profile.

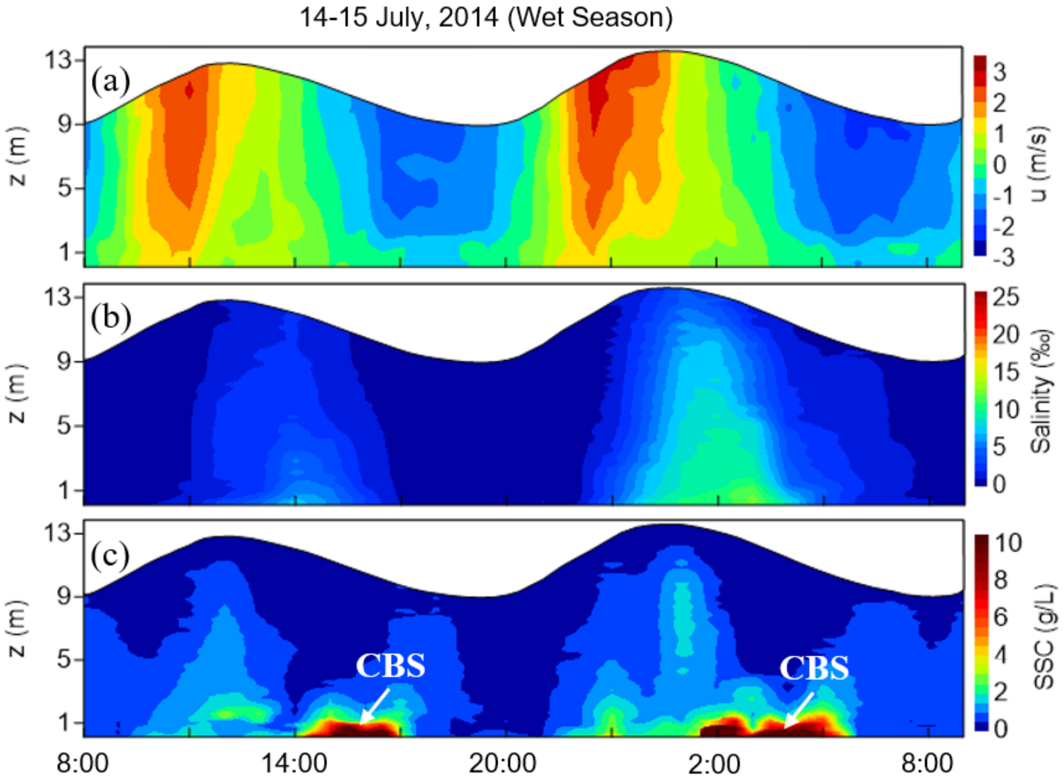

Figure 10. Time-depth variability of (a) along-channel velocity (u), (b) salinity and (c) SSC during 14-15 July, 2014. Positive u indicates the flood direction. CBS denotes the concentrated benthic suspension (SSC > 10 g/L).

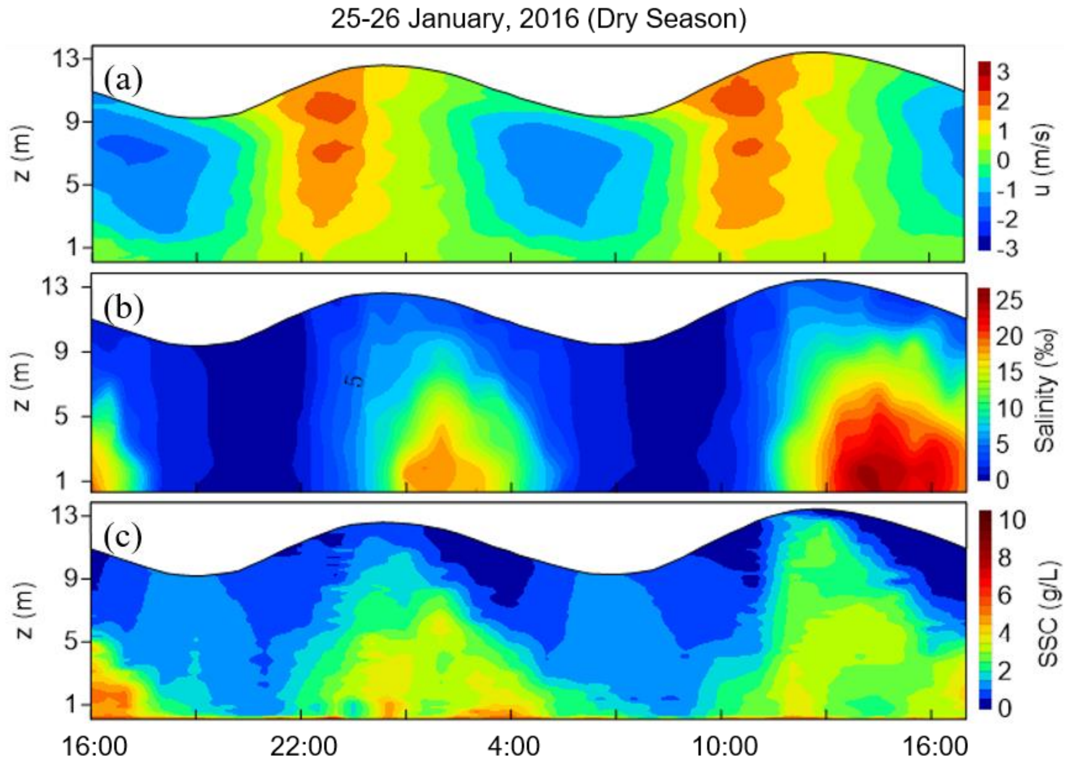

Figure 11. Time-depth variability of (a) along-channel velocity (u), (b) salinity and (c) SSC during 25-26 January, 2016. Positive u indicates the flood direction.

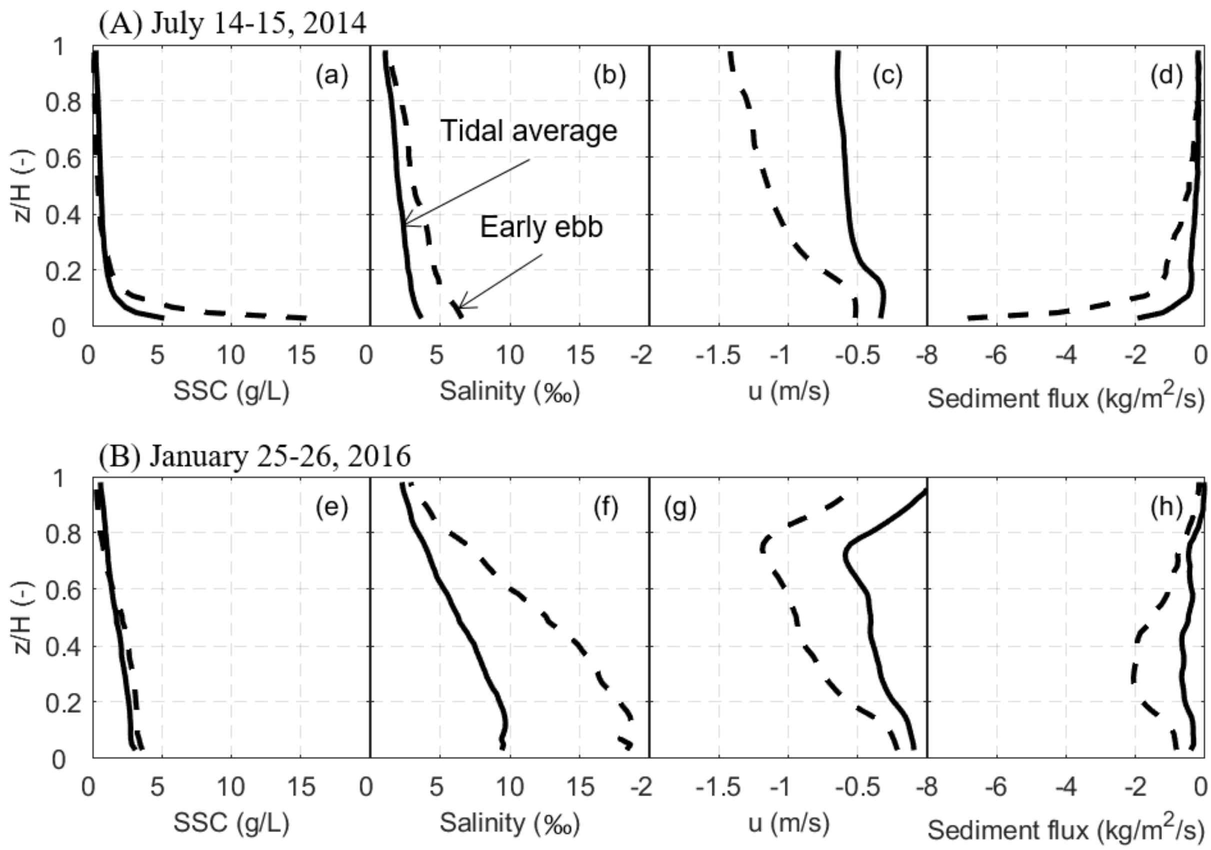

Figure 12. Profiles of (a) (e) SSC, (b) (f) salinity, (c) (g) along-channel velocity (u) and (d) (h) along-channel sediment flux averaged over tidal cycles (solid line) and early ebb (dash line) of spring tide in July, 2014 (upper panels) and January, 2016 (lower panels). Negative u and flux indicate the direction from land to sea.

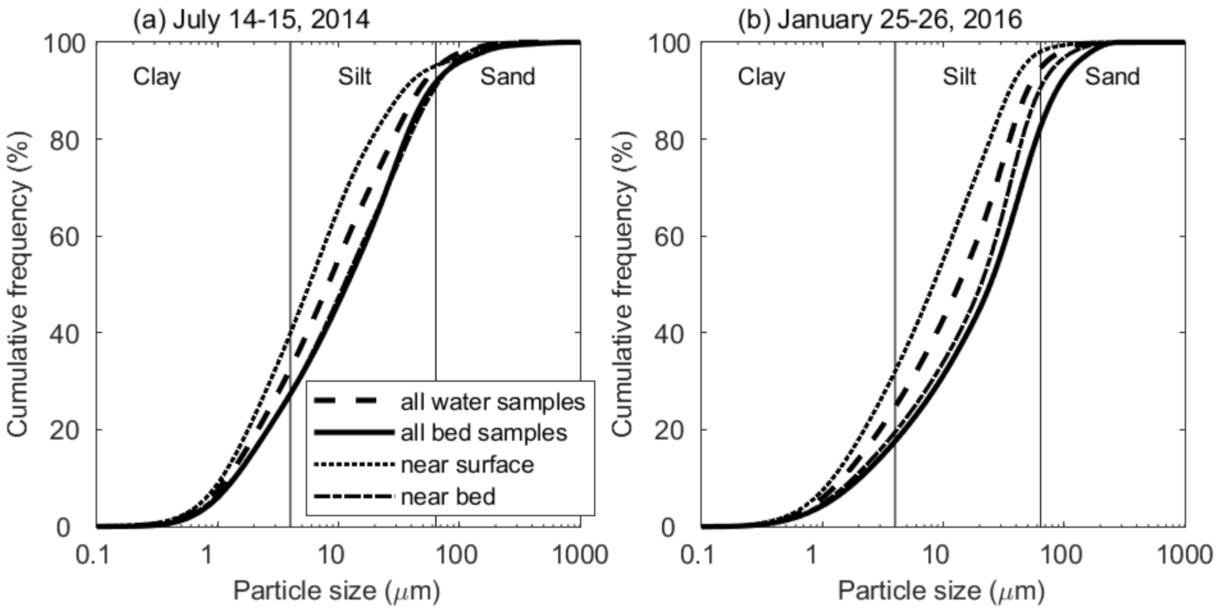

Figure 13. The cumulative frequency distribution of the sediment samples collected near water surface (dot), near seabed (dash dot), and at seabed surface (solid) in July, 2014 (a) and January, 2016 (b). The dash line represents the average of all water samples.